

## corrections

### Experimental verification of the quasi-unit-cell model of quasicrystal structure

Paul J. Steinhart, H.-C. Jeong, K. Saitoh, M. Tanaka, E. Abe & A. P. Tsai

*Nature* 396, 55–57 (1998)

Figure 3 of this Letter wrongly shows all cobalt sites as yellow filled circles, indicating that they lie on the same  $c = 0$  level, whereas the two lower sites in the figure were intended to be open circles, indicating cobalt sites on the  $c = 1/2$  level. A corrected version of the figure can be found on *Nature's* website.

### Extreme Th1 bias of invariant $V\alpha 24J\alpha Q$ T cells in type 1 diabetes

S. Brian Wilson, Sally C. Kent, Kurt T. Patton, Tihamer Orban, Richard A. Jackson, Mark Exley, Steven Porcelli, Desmond A. Schatz, Mark A. Atkinson, Steven P. Balk, Jack L. Strominger & David A. Hafler

*Nature* 391, 177–181 (1998)

In this Letter, we reported that invariant  $V\alpha 24J\alpha Q$  T cells from monozygotic diabetic twins/triplets were reduced in number and produced only interferon- $\gamma$  on appropriate stimulation, whereas those cloned from at-risk non-diabetic twins/triplets and controls produced both interferon- $\gamma$  and interleukin(IL)-4. We also reported (see our Fig. 4) that 50% (7/14) of high-risk diabetes non-progressors had markedly raised levels of serum IL-4, as measured by ELISA. However, we now find that measurement of serum IL-4 by ELISA is confounded by the presence in some serum samples of a heterophile-like substance(s) that gives false positive estimations for IL-4 by crosslinking the capture and detection antibodies used in the assay<sup>1,2</sup>. This is not the case when IL-4 is measured in the tissue-culture medium of *in vitro* activated T cells. Details will be published once the source of error is determined, a method for accurate measurement of serum IL-4 is established, and the apparent association of production of the heterophile substance and/or IL-4 with diabetic non-progression has been clarified. □

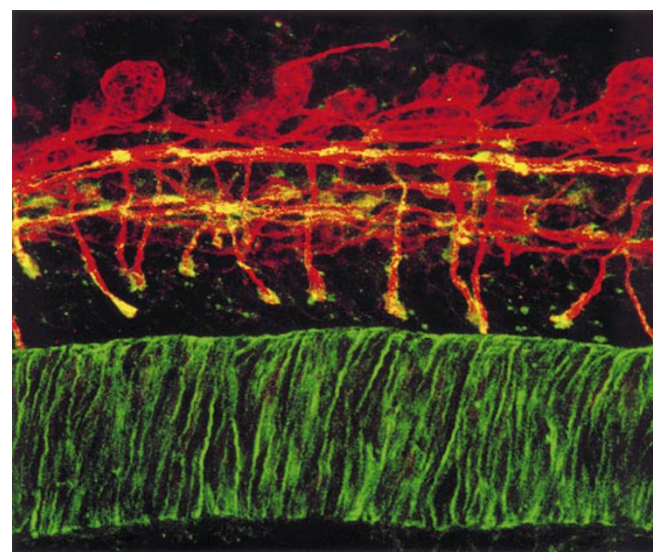
1. Redondo, M. *et al.* *Diabetes* 48 (suppl. 1) Abstr. (1999).
2. Ellis, T. *et al.* *Diabetes* 48 (suppl. 1) Abstr. (1999).

### *In vivo* regulation of axon extension and pathfinding by growth-cone calcium transients

Timothy M. Gomez & Nicholas C. Spitzer

*Nature* 397, 350–355 (1999)

The cover image on this issue should have been orientated as shown here to conform with the location of the notochord as described in the cover caption. □



### The role of mat-forming diatoms in the formation of Mediterranean sapropels

Alan E. S. Kemp, Richard B. Pearce, Itaru Koizumi, Jennifer Pike & S. Jae Rance

*Nature* 398, 57–61 (1999)

In this Letter, the legend to Fig. 2 has the descriptions switched for the last two panels. The image shown in Fig. 2c is in fact of *H. hauckii*, with scale bar 20  $\mu\text{m}$ , and that in Fig. 2d is of *P. calcar-avis*, with scale bar 10  $\mu\text{m}$ .

10. Ernst, R., Bodenhausen, G. & Wokaun, A. *Principles of Nuclear Magnetic Resonance in One and Two Dimensions* (Oxford Univ. Press, 1990).
11. Grant, D. M. & Harris, R. K. (eds) *Encyclopedia of Nuclear Magnetic Resonance* (Wiley, New York, 1996).
12. Gershenfeld, N. & Chuang, I. L. Bulk spin resonance quantum computation. *Science* **275**, 350–356 (1997).
13. Cory, D. G., Price, M. D. & Havel, T. F. Nuclear magnetic resonance spectroscopy: An experimentally accessible paradigm for quantum computing. *Physica D* **120**, 82–101 (1998).
14. Laflamme, R., Knill, E., Zurek, W. H., Catásti, P. & Mariappan, S. V. S. NMR Greenberger-Horne-Zeilinger states. *Phil. Trans. R. Soc. Lond. A* **356**, 1941–1947 (1998).
15. Cory, D. G. *et al.* Experimental quantum error correction. *Phys. Rev. Lett.* **81**, 2152–2155 (1998).
16. Chuang, I. L., Gershenfeld, N. & Kubinec, M. Experimental implementation of fast quantum searching. *Phys. Rev. Lett.* **18**, 3408–3411 (1998).
17. Jones, J. A. & Mosca, M. Implementation of a quantum algorithm on a nuclear magnetic resonance quantum computer. *J. Chem. Phys.* **109**, 1648–1653 (1998).
18. Chuang, I. L., Vandersypen, L. M. K., Zhou, X. L., Leung, D. W. & Lloyd, S. Experimental realization of a quantum algorithm. *Nature* **393**, 143–146 (1998).
19. Jones, J. A., Mosca, M. & Hansen, R. H. Implementation of a quantum search algorithm on a nuclear magnetic resonance quantum computer. *Nature* **393**, 344–346 (1998).
20. Brassard, G., Braunstein, S. & Cleve, R. Teleportation as a quantum computation. *Physica D* **120**, 43–47 (1998).
21. Zurek, W. H. Decoherence and the transition from quantum to classical. *Phys. Today* **44**, 36–44 (1991).
22. Schumacher, B. W. Sending entanglement through noisy quantum channels. *Phys. Rev. A* **54**, 2614–2628 (1996).
23. Barnum, H., Nielsen, M. A. & Schumacher, B. W. Information transmission through a noisy quantum channel. *Phys. Res. A* **57**, 4153–4175 (1998).
24. Poyatos, J. F., Cirac, J. I. & Zoller, P. Complete characterization of a quantum process: the two-bit quantum gate. *Phys. Rev. Lett.* **78**, 390–393 (1997).
25. Chuang, I. L. & Nielsen, M. A. Prescription for experimental determination of the dynamics of a quantum black box. *J. Mod. Opt.* **44**, 2455–2467 (1997).
26. Nielsen, M. A. & Caves, C. M. Reversible quantum operations and their application to teleportation. *Phys. Rev. A* **55**, 2547–2556 (1997).
27. Furusawa, A. *et al.* Unconditional quantum teleportation. *Science* (in the press).

**Acknowledgements.** We thank D. Cory, C. Jarzynski, J. Ye and W. Zurek for discussions, the Stable Isotope Laboratory at Los Alamos for use of their facility, and the National Security Agency and Office of Naval Research for support.

Correspondence and requests for materials should be addressed to M.A.N. (e-mail: mnielsen@theory.caltech.edu).

## Experimental verification of the quasi-unit-cell model of quasicrystal structure

Paul J. Steinhardt\*, H.-C. Jeong†, K. Saitoh‡, M. Tanaka‡, E. Abe§ & A. P. Tsai§

\* Department of Physics, Princeton University, Princeton, New Jersey 08544, USA

† Department of Physics, Sejong University, Kwangjin, Seoul 143-747, Korea

‡ Research Institute for Scientific Measurements, Tohoku University,

2-1-1 Katahira, Aoba-ku, Sendai 980-8577, Japan

§ National Research Institute for Metals, 1-2-1 Sengen, Tsukuba, Ibaraki 305-0047, Japan

The atomic structure of quasicrystals<sup>1</sup>—solids with long-range order, but non-periodic atomic lattice structure—is often described as the three-dimensional generalization of the planar two-tile Penrose pattern<sup>2</sup>. Recently, an alternative model has been proposed<sup>3–5</sup> that describes such structures in terms of a single repeating unit<sup>3–5</sup>—the three-dimensional generalization of a pattern composed of identical decagons. This model is similar in concept to the unit-cell description of periodic crystals, with the decagon playing the role of a ‘quasi-unit cell’. But, unlike the unit cells in periodic crystals, these quasi-unit cells overlap their neighbours, in the sense that they share atoms. Nevertheless, the basic concept of unit cells in both periodic crystals and quasicrystals is essentially the same: solving the entire atomic structure of the solid reduces to determining the distribution of atoms in the unit cell. Here we report experimental evidence for the quasi-unit-cell model by solving the structure of the decagonal quasicrystal  $\text{Al}_{72}\text{Ni}_{20}\text{Co}_8$ . The resulting structure is consistent with images obtained by electron and X-ray diffraction, and agrees with the measured stoichiometry, density and symmetry of the compound. The quasi-unit-cell model provides a significantly better fit to these results than all previous alternative models, including Penrose tiling.

The fact that the entire structure reduces to a single repeating unit means that quasicrystals have a simplicity more like that of crystals than previously recognized. The quasi-unit-cell picture also suggests reasons why quasicrystals may form instead of crystals under some conditions. For the two-dimensional analogue, a pattern composed of overlapping decagonal quasi-unit cells, Gummelt<sup>3</sup> and Steinhardt and Jeong<sup>4,5</sup> have proved that the quasicrystal pattern is uniquely forced if decagons only overlay according to the rules shown in Fig. 1a. Steinhardt and Jeong<sup>4,5</sup> have further proved that the quasi-unit-cell structure can arise simply by maximizing the density of a chosen cluster of atoms. If one imagines that the atomic cluster is energetically preferred, then the quasicrystal could be the ground-state configuration as minimizing the free energy maximizes the cluster density. Establishing the correspondence between quasi-unit cells and real atomic structures opens the door to theoretical and empirical tests of these notions.

The quasi-unit-cell and Penrose-tile pictures are examples of real-space descriptions of quasicrystals in which the structure is defined by decorating each quasi-unit cell or each type of tile identically. Some Penrose-tile models are based on the two-tile rhombus or kite-and-dart sets; others are based on the six-tile pentagonal set. In the hyperspace description, the quasicrystal is viewed as a projection from a higher-dimensional periodic, hypercubic lattice and the atomic decoration is defined in terms of atomic surfaces in the higher-dimensional space (five or six dimensions) which project into point atoms in three dimensions<sup>6</sup>. The surfaces may be continuous, discontinuous, or even fractal. Depending on the surfaces, the surfaces may produce a structure equivalent to decorating all tiles (or quasi-unit cells) identically or to decorating tiles differently depending on their local environment. Although the descriptions are mathematically related, the quasi-unit-cell picture is simpler in practice: it is much easier to solve for the structure by considering atomic rearrangements within a single quasi-unit cell in real, three-dimensional space than by considering simultaneously decorations or two or more tiles or by imagining surfaces in five or six dimensions.

To test the quasi-unit-cell hypothesis, we consider  $\text{Al}_{72}\text{Ni}_{20}\text{Co}_8$ , one of the best-characterized quasicrystal materials.  $\text{Al}_{72}\text{Ni}_{20}\text{Co}_8$  is an example of a decagonal phase; that is, a structure consisting of a periodic stack of ten-fold symmetric quasiperiodically ordered layers. Viewed along the periodic axis, the solid has the same symmetry as a Penrose tiling or an overlapping decagon structure. Hence it can be modelled as a columnar stacking of prisms with the shapes of Penrose tiles or decagons. Although quasicrystalline Al–Ni–Co has been studied for nearly a decade, deciphering its structure has been challenging for materials science reasons. The quasicrystal phase was originally found in a wide compositional range<sup>7</sup>. High-resolution transmission electron microscopy revealed decagonal cluster columns roughly 2 nm across<sup>8</sup>. Models of the structure based on two Penrose rhombus tiles, the Penrose six-tile pentagonal set<sup>9,10</sup> and random packing of decagons were proposed on the basis of this early data<sup>11</sup>. In random packing, there are no rules which force the decagons into a unique structure, so infinitely many distinct configurations are possible. (Similar random cluster packing models have been developed for other quasicrystalline materials with decagonal and icosahedral symmetry<sup>12–14</sup>.) Although the random cluster packing models and the quasi-unit-cell picture discussed here share the idea of building the atomic structure from a repeating unit, they differ in three important ways: first, the random decagon clusters do not cover the entire structure; second, the random decagon clusters are imperfectly ordered and their arrangement is not unique; and third (in most cases), the random decagon clusters contain an atomic configuration that is five- or ten-fold symmetric.

But it has recently become apparent that, over most of the compositional and temperature range, one obtains an inhomogeneous mixture of structures<sup>15–17</sup>. The ideal, high-perfection phase

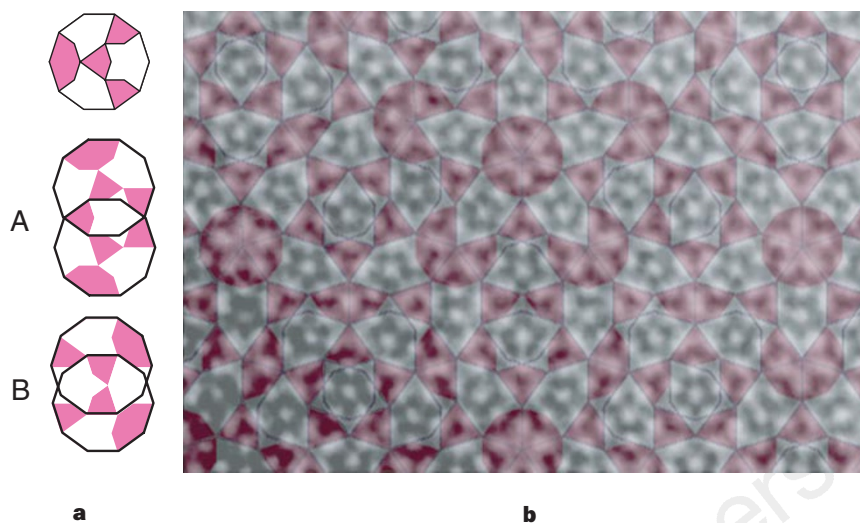


**Figure 1** Comparison of atomic lattice image and quasi-unit-cell picture. **a**, The decagon quasi-unit cell with coloured kite-shapes indicating overlap rules (overlapping regions must have matching colour); only 'A' or 'B' overlaps are permitted. **b**, Two overlaying images. In black and white is the high-angle annular dark-field (HAADF) image of  $\text{Al}_{72}\text{Ni}_{20}\text{Co}_8$  in which decagonal rings of atoms are evident. To obtain an objective measure, we digitized the image and performed a random search for rings of ten atoms (white spots) of the type shown in Fig. 2. Allowing modest tolerance for distortion and digitization error, the random search

converged on a set of decagons that cover the entire image. The decagon covering has been superposed over the HAADF image in **b**. All decagons overlap neighbours according to A or B overlaps and the decagon tiling is a perfect quasiperiodic pattern. Furthermore, the decagon interiors have been coloured with the kite-shapes which serve as mnemonics for the overlap rules, as shown in **a**. In **b**, there is near-perfect correspondence between the atomic decorations of both the decagons and the kite-regions.

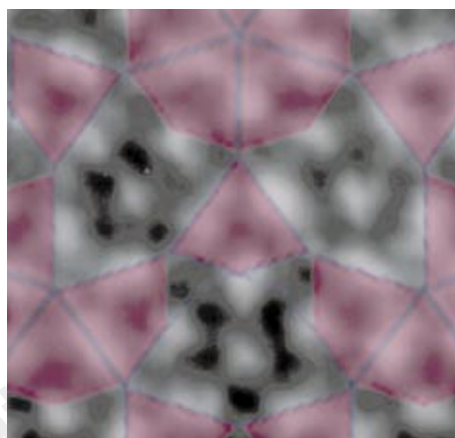


**Figure 2** Magnified view of decagon cluster displaying broken symmetry. A magnified view of a decagonal cluster from Fig. 1 illustrating a decagonal ring of atoms (at edge-centres of decagon) and showing how the three bright spots in the middle of the decagonal cluster break decagonal symmetry in a way similar to the kite-representation of the overlap rules.

has a composition  $\text{Al}_{72}\text{Ni}_{20}\text{Co}_8$ , significantly different from the samples on which previous models were based. Whereas earlier samples exhibited diffuse scattering and superlattice reflections in the diffraction patterns,  $\text{Al}_{72}\text{Ni}_{20}\text{Co}_8$  does not. The phase is stable and reproducible at temperatures of about  $800^\circ\text{C}$ , and highly perfect water-quenched samples can be grown as large as 1 mm. So it is only now that precise measurements of the structure, stoichiometry and density of this material have become possible, which provide powerful new constraints on models. Previous models fail badly on all counts. (Saitoh has recently developed a model based on two kinds of pentagon clusters<sup>18,19</sup>—the first to reproduce the observed breaking of ten-fold symmetry inside the 2-nm clusters and to obtain the correct space-group symmetry—but his model does not match the measured density or stoichiometry.)

To test the quasi-unit-cell picture, we have performed the following tests.

(1) *Decagon overlap test*. In the quasi-unit-cell picture, the structure

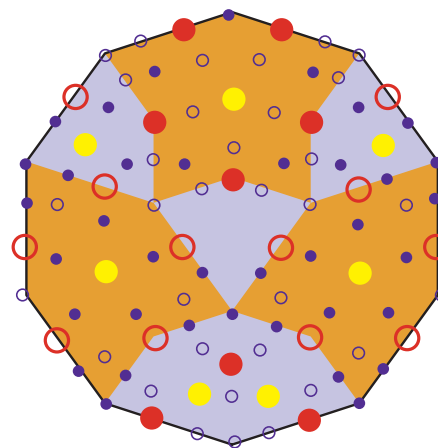


**Figure 3** The best-fit candidate model for the atomic decoration of the decagonal quasi-unit cell for  $\text{Al}_{72}\text{Ni}_{20}\text{Co}_8$ . Large circles represent Ni (red) or Co (yellow) and small circles represent Al. The structure has two distinct layers along the periodic  $c$ -axis. Solid circles represent  $c = 0$  and open circles represent  $c = 1/2$ . The experimental input used to generate candidate models is: (1) the space group  $P10_5/mmc$  based on convergent-beam electron-diffraction methods<sup>18</sup>; (2) the HAADF image, in which scattering is proportional to the square of the atomic number, highlights the positions of the transition metals relative to the aluminium; and (3), based on X-ray diffraction, the diameter of the decagonal cluster is 2.033 nm and the period along the decagonal  $c$ -axis is 0.408 nm, corresponding to two atomic layers per period. To obtain  $P10_5/mmc$ , different atomic arrangements are placed on the two layers along the  $c$ -axis such that two overlapping decagons related by odd-multiple rotations of  $\pi/10$  must be shifted by a half-period in order to share atoms. Thus the covering of the plane can be decomposed into two interpenetrating lattices of decagons, in which the decagon decoration in one set is related by screw symmetry or  $c$ -glide symmetry with respect to the other. Using positions of the transition metals inferred from the HAADF images, a sequence of plausible decagon decorations was explored and the best fits to the experimentally measured stoichiometry and density ( $3.94 \text{ g cm}^{-3} \pm 1\%$ ) were found. For each decoration, the constraint had to be imposed that shared atoms at overlapping sites were identical.



consists of a covering by a single, repeating decagonal cluster (column) which overlaps (shares atoms with) neighbours in two, and only two, distinct ways ('A' and 'B'), according to the overlap rules<sup>4</sup> shown in Fig. 1a. In Fig. 1b, we digitized the high-angle annular dark-field (HAADF) image<sup>18</sup> of  $\text{Al}_{72}\text{Ni}_{20}\text{Co}_8$  and searched randomly for decagonal rings of atoms (white spots). The random search converged on a set of decagons that cover the entire image in a perfect quasiperiodic pattern in which all decagons overlap neighbours according to A or B overlaps.

(2) *Broken decagonal symmetry test.* In Fig. 1a, the decagon interior has been coloured with kite-shapes which break ten-fold symmetry. The kite-shapes serve as mnemonics for the overlap rule. Figure 2 is a magnified view of one decagon from Fig. 1b which shows that the central triangle of atoms breaks the ten-fold symmetry<sup>18,20</sup> in a way that is isomorphic to the kite-shapes. The correspondence is maintained throughout Fig. 1b. In principle, one could have overlapping decagons with ten-fold (or five-fold) symmetric decorations; however, the broken symmetry is significant because it suggests that overlap rules may play a role in determining the atomic arrangements.

(3) *Stoichiometry/density/space-group tests.* For any candidate model of  $\text{Al}_{72}\text{Ni}_{20}\text{Co}_8$ , the atomic structure is totally determined by the atomic decoration of the decagonal quasi-unit cell. Steinhardt and Jeong (manuscript in preparation) have developed a procedure for computing the stoichiometry, density and symmetry given the atomic decoration of the quasi-unit cell. The procedure is non-trivial because neighbouring cells share atoms, and double-counting must be avoided. This procedure was used to compare models with the experimentally determined stoichiometry, density and symmetry. Figure 3 is, by a significant margin, the best-fit model. The density of  $3.97 \text{ g cm}^{-3}$  and the stoichiometry of  $\text{Al}_{72.5}\text{Ni}_{18.6}\text{Co}_{8.9}$  are both within the reported experimental uncertainties and the space-group symmetry is correct. For this material, the best-fit model happens to be one which cannot be described as a simple decoration of a Penrose rhombus tiling in which each type of tile is

decorated identically. Decorations of Penrose tiles are a proper subset of the possible decorations of (decagon) quasi-unit cells (P.J.S. and H.-C.J., manuscript in preparation) and so they are automatically included in our analysis. No Penrose model satisfying the HAADF and symmetry constraints was found which matched the measured stoichiometry and density.

(4) *HREM image test.* We computed high-resolution electron microscopy (HREM) images for our best-fit model, and compared them with experimental images. Figure 4 shows that the agreement is excellent. This test is somewhat independent of the first test because HREM images include contributions of both aluminum and transition-metal atoms, whereas HAADF images display prominently only transition metals.

The quasi-unit-cell picture for the decagonal phase of  $\text{Al}_{72}\text{Ni}_{20}\text{Co}_8$  has passed all currently possible tests; it satisfies more constraints than previous atomic models for  $\text{Al}_{72}\text{Ni}_{20}\text{Co}_8$  (or other quasicrystals) and provides a significantly better fit than previous approaches. We believe that other decagonal quasicrystals will also fit well. For example, a new class of stable decagonal quasicrystals belonging to the Frank-Kasper family have been discovered, including  $\text{ZnMgDy}$  (ref. 21), which also produce images composed of overlapping decagonal clusters whose internal structure breaks decagonal symmetry in accordance with the overlap rules. The ultimate aim is to move beyond using the quasi-unit-cell picture to describe the structure, and to begin to explain why the structure forms in the first place. The quasi-unit-cell picture suggests that the key is understanding the energetics of the repeating atomic cluster: deciphering quasicrystals in terms of quasi-unit cells should therefore provide realistic data to test theories of why quasicrystals form. □

Received 8 July; accepted 19 August 1998.

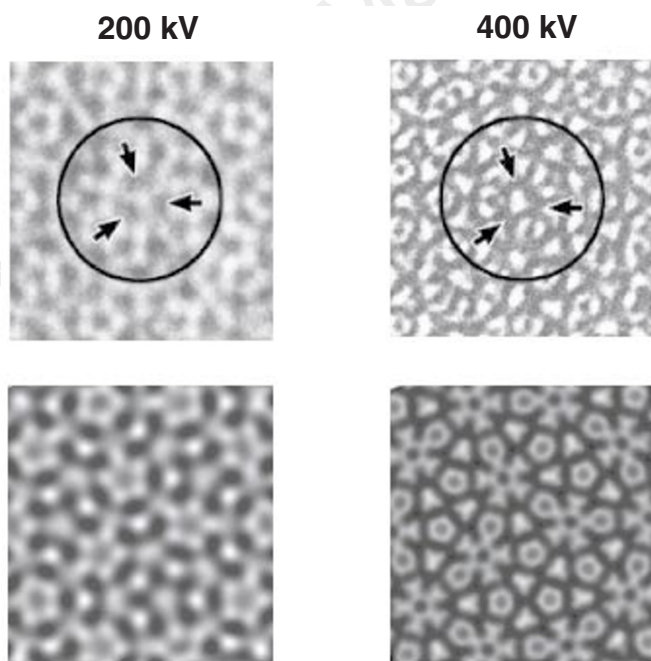


**Figure 4** Comparison of experimental lattice images with computed image for best-fit model. A comparison of the high-resolution electron microscope images of  $\text{Al}_{72}\text{Ni}_{20}\text{Co}_8$  (top row) at accelerating voltages of 200 kV (obtained by Hiraga *et al.*<sup>8</sup>) and 400 kV (obtained by Saitoh *et al.*<sup>19</sup>), compared to computed images (bottom row) for the candidate model in Fig. 3. The images were computed using the software package MacTempas (Total Resolution Inc., Berkeley, CA). Allowing for minor imperfections in the experimental sample and our inability to match precisely the observational conditions, the correspondence is very close.

- Levine, D. & Steinhardt, P. J. Quasicrystals: a new class of ordered structures. *Phys. Rev. Lett.* **53**, 2477–2480 (1984).
- Penrose, R. The role of aesthetics in pure and applied mathematical research. *Bull. Inst. Math. Applic.* **10**, 266–271 (1974).
- Gummelt, P. Construction of Penrose tilings by a single aperiodic prototile. *Geometriae Dedicata* **62**, 1–17 (1996).
- Steinhardt, P. J. & Jeong, H.-C. A simpler approach to Penrose tiling with implications for quasicrystal formation. *Nature* **382**, 433–435 (1996).
- Jeong, H.-C. & Steinhardt, P. J. Constructing Penrose-like tilings from a single proto-tile and the implications for quasicrystals. *Phys. Rev. B* **55**, 3520–3532 (1997).
- Janot, C. & de Boissieu, M. in *Quasicrystals: The State of the Art* (eds DiVincenzo, D. & Steinhardt, P. J.) 57–94 (World Scientific, Singapore, 1995).
- Tsai, A. P., Inoue, A. & Masumoto, T. Icosahedral, decagonal and amorphous phases in Al–Cu–M (M = transition metal) systems. *Mater. Trans. Jpn Inst. Metals* **30**, 666–676 (1989).
- Hiraga, K., Lincoln, E. J. & Sun, W. Structure and structural change of Al–Ni–Co decagonal quasicrystal by high-resolution electron microscopy. *Mater. Trans. Jpn Inst. Metals* **32**, 308–314 (1991).
- Yamamoto, A. Structure of decagonal  $\text{Al}_{65}\text{Cu}_{20}\text{Co}_{15}$  quasicrystals. *Sci. Rep. Res. Inst. Tohoku Univ. A* **42**, 207–212 (1996).
- Ritsch, S. *et al.* Highly perfect decagonal Al–Co–Ni quasicrystals. *Phil. Mag. A* **74**, 99–106 (1996).
- Burkov, S. Modeling decagonal quasicrystals: random assembly of interpenetrating decagonal clusters. *J. Phys.* **2**, 695–706 (1992); Structure model of the Al–Cu–Co decagonal quasicrystal. *Phys. Rev. Lett.* **67**, 614–617 (1991).
- Steurer, W. & Kuo, K. H. Five-dimensional structure analysis of decagonal  $\text{Al}_{65}\text{Cu}_{20}\text{Co}_{15}$ . *Acta Crystallogr. B* **46**, 703–712 (1990).
- Boudard, M. *et al.* Atomic structure of the Al–Pd–Mn icosahedral phase. *J. Non-Cryst. Solids* **153–4**, 5–9 (1993).
- Janot, C. & Patera, J. Simple physical generation of quasicrystals. *Phys. Lett. A* **233**, 110–114 (1997).
- Edagawa, K., Ichihara, M., Suzuki, K. & Takeuchi, S. New type of decagonal quasicrystal with superlattice order in Al–Ni–Co alloy. *Phil. Mag. Lett.* **66**, 19–25 (1992).
- Ritsch, S., Beeli, C., Nissen, H.-U. & Luck, R. Two different superstructures of the decagonal Al–Co–Ni quasicrystal. *Phil. Mag. A* **71**, 671–685 (1995).
- Fujiwara, A., Tsai, A. P. & Inoue, A. in *Proc. 6th Int. Conf. Quasicrystals* (eds Takeuchi, S. & Fujiwara, A.) 341 (World Scientific, Singapore, 1988).
- Saitoh, K., Tsuda, K., Tanaka, M., Kaneko, K. & Tsai, A. P. Structural study of an  $\text{Al}_{72}\text{Ni}_{20}\text{Co}_8$  decagonal quasicrystal using the high-angle annular dark-field method. *Jpn J. Appl. Phys.* **36**, L1400–L1402 (1997).
- Saitoh, K., Tsuda, K. & Tanaka, M. A new structural model of an  $\text{Al}_{72}\text{Ni}_{20}\text{Co}_8$  decagonal quasicrystal. Preprint (Tohoku Univ., 1998); *J. Phys. Soc. Jpn.* (in the press).
- Beeli, C. & Horiuchi, S. The structure and its reconstruction in the decagonal  $\text{Cl}_{70}\text{Cu}_{17}\text{Co}_{13}$ . *Phil. Mag. B* **70**, 215–240 (1994).
- Sato, T. J., Abe, E. & Tsai, A. P. A novel decagonal quasicrystal in Zn–Mg–Dy system. *Jpn J. Appl. Phys.* **36**, L1038–L1039 (1997).
- Mermin, N. D. in *Quasicrystals: The State of the Art* (eds DiVincenzo, D. & Steinhardt, P. J.) 133–184 (World Scientific, Singapore, 1991).

**Acknowledgements.** We thank R. Kilaas of Total Resolution, Inc. for lending us the MacTempas software package for this project. This work was partially supported by the US Department of Energy at Princeton, and by CREST (Core Research for Evolutional Science and Technology) of Japan Science and Technology Corporation (JST).

Correspondence and requests for materials should be addressed to P.J.S. (e-mail: steinh@princeton.edu).

type (+/+) sibling of the same sex from the same litter. Locomotion experiments were run by an observer blind to the genotype of the animals being tested. Tests were run from 10 a.m. to 2 p.m. Data are presented as mean  $\pm$  s.e.m. Statistical analysis was performed using ANOVA (\* $P$  < 0.05 mutant compared with wild type).

**Self-administration.** Adult male mice (wild-type and mutant siblings of parents backcrossed 3 generations to C57 B1/6 inbred mice) were implanted with a silastic catheter in the jugular vein under halothane anaesthesia and tested in operant cages equipped with two nose-poke detectors, one active, the other inactive (V. Deroche *et al.*, manuscript in preparation). All mice were first trained with cocaine (0.8 mg kg<sup>-1</sup> per injection, delivered in 50  $\mu$ l per 2 s, with 20-s time-out period) under fixed-ratio (FR) 1 for 2–4 sessions, then under FR2 until stable baseline was reached. Spontaneous nose-poke behaviour, measured in naive, sham-operated mice when both detectors were inactive, was low and non-discriminatory ( $2.6 \pm 0.6$  per h), and did not differ between  $\beta 2^{-/-}$  mice and wild-type mice (not shown). The baseline for each mouse was defined as 3 consecutive sessions with less than 30% deviation from the mean and at least 75% active-specific response. During 5 consecutive daily sessions, cocaine was replaced with nicotine (0.03 mg kg<sup>-1</sup> per injection, delivered in 50  $\mu$ l per 2 s, 20-s time-out period, under FR 2 schedule) in wild-type mice ( $n = 5$ ) and  $\beta 2^{-/-}$  mice ( $n = 5$ ). In a second group of wild-type mice ( $n = 5$ ), cocaine was replaced with saline, forcing the operant responding to extinction. Cocaine and nicotine bitartrate (Sigma) were freshly dissolved in saline before each experiment.

**Equilibrium binding.** Receptor autoradiography was done as described<sup>19–21</sup>. Briefly, following 30 min preincubation in the appropriate buffer, 14- $\mu$ m coronal brain sections from wild-type and  $\beta 2$ -mutant mice were incubated at room temperature for 120 min with 5 nM [<sup>3</sup>H]WIN35,428 (84.5 Ci mmol<sup>-1</sup>; NEN)<sup>19</sup> or for 60 min with either 1.5 nM SCH23390 (70 Ci mmol<sup>-1</sup>; NEN)<sup>20</sup> or 3 nM raclopride (82.4 Ci mmol<sup>-1</sup>; NEN)<sup>21</sup>. Slides were washed in ice-cold buffer twice for 1 min (WIN35,428) or for 5 min (SCH23390 or raclopride), and exposed to hyperfilm together with appropriate standards ([<sup>3</sup>H]microscale; Amersham). Nonspecific labelling was determined in the presence of 30  $\mu$ M cocaine for the dopamine transporter and 1  $\mu$ M (+)butaclamol for D1 and D2. Siblings of the same sex and litter were used for all experiments ( $n$ , 4–6 per group).

**Cyclase and tyrosine hydroxylase assays.** Dopamine-stimulated cyclase activity was measured in striatal homogenates from wild-type and  $\beta 2$ -mutant siblings of the same sex and same litter by following published protocols<sup>22</sup> and using the Amersham Biotrak scintillation proximity assay to determine cAMP levels. For each animal ( $n = 6$  per group), the striatum from one side of the brain was used for dopamine-stimulated cyclase assays, and the striatum from the other side of the brain was used to measure tyrosine hydroxylase activity as described<sup>23</sup>. Briefly, after homogenization, samples were incubated with [<sup>3</sup>H]tyrosine and tetrahydrobiopterin. End products were separated from unreacted [<sup>3</sup>H]tyrosine by treatment with activated charcoal. Results are reported as the number of counts incorporated minus background per  $\mu$ g protein assayed.

Received 7 August; accepted 25 September 1997.

- Dani, J. A. & Heinemann, S. Molecular and cellular aspects of nicotine abuse. *Neuron* **16**, 905–908 (1996).
- Role, L. W. & Berg, D. K. Nicotinic receptors in the development and modulation of CNS synapses. *Neuron* **16**, 1077–1085 (1996).
- Picciotto, M. R. *et al.* Abnormal avoidance learning in mice lacking functional high-affinity nicotine receptor in the brain. *Nature* **374**, 65–67 (1995).
- Koob, G. F. Drugs of abuse: anatomy, pharmacology and function of reward pathways. *Trends Pharmacol. Sci.* **13**, 177–184 (1992).
- Stolerman, I. P., Mirza, N. R. & Shoaib, M. Nicotine psychopharmacology: Addiction, cognition and neuroadaptation. *Med. Res. Rev.* **15**, 47–72 (1995).
- Pontieri, E. E., Tanda, G., Orzi, F. & Di Chiara, G. Effects of nicotine on the nucleus accumbens and similarity to those of addictive drugs. *Nature* **382**, 255–257 (1996).
- Grady, S., Marks, M. J., Wonnacott, S. & Collins, A. C. Characterization of nicotinic receptor-mediated [<sup>3</sup>H]dopamine release from synaptosomes prepared from mouse striatum. *J. Neurochem.* **59**, 848–856 (1992).
- Clarke, P. B., Fu, D. S., Jakubovic, A. & Fibiger, H. C. Evidence that mesolimbic dopaminergic activation underlies the locomotor stimulant action of nicotine in rats. *J. Pharmacol. Exp. Ther.* **246**, 701–708 (1988).
- Corrigall, W. A., Franklin, K. B., Coen, K. M. & Clarke, P. B. The mesolimbic dopaminergic system is implicated in the reinforcing effects of nicotine. *Psychopharmacology (Berlin)* **107**, 285–289 (1992).
- Le Novère, N., Zoli, M. & Changeux, J.-P. Neuronal nicotinic receptor  $\alpha 6$  subunit mRNA is selectively concentrated in catecholaminergic nuclei of the rat brain. *Eur. J. Neurosci.* **8**, 2428–2439 (1996).
- Reavill, C., Walther, B., Stolerman, I. P. & Testa, B. Behavioural and pharmacokinetic studies on nicotine, cytosine and lobeline. *Neuropharmacology* **29**, 619–624 (1990).
- Risinger, F. O. & Oakes, R. A. Nicotine-induced conditioned place preference and conditioned place aversion in mice. *Pharmacol. Biochem. Behav.* **51**, 457–461 (1995).

- Nisell, M., Nomikos, G. G. & Svensson, T. H. Systemic nicotine-induced dopamine release in the rat nucleus accumbens is regulated by nicotinic receptors in the ventral tegmental area. *Synapse* **16**, 36–44 (1994).
- Henningfield, J. E., Miyasato, K. & Jasinski, D. R. Cigarette smokers self-administer intravenous nicotine. *Pharmacol. Biochem. Behav.* **19**, 887–890 (1983).
- Reavill, C., Walther, B., Stolerman, I. P. & Testa, B. Behavioural and pharmacokinetic studies on nicotine, cytosine and lobeline. *Neuropharmacology* **29**, 619–624 (1990).
- Grace, A. A. & Onn, S. P. Morphology and electrophysiological properties of immunocytochemically identified rat dopamine neurons recorded *in vitro*. *J. Neurosci.* **9**, 3463–3481 (1989).
- Luetje, C. W. & Patrick, J. Both  $\alpha$ - and  $\beta$ -subunits contribute to the agonist sensitivity of neuronal nicotinic acetylcholine receptors. *J. Neurosci.* **11**, 837–845 (1991).
- Izenwasser, S., Jacobs, H. M., Rosenberger, J. G. & Cox, B. M. Nicotine indirectly inhibits [<sup>3</sup>H]dopamine uptake at concentrations that do not directly promote [<sup>3</sup>H]dopamine release in rat striatum. *J. Neurochem.* **56**, 603–610 (1991).
- Kaufman, M. J., Spelman, R. D. & Madras, B. K. Distribution of cocaine recognition sites in monkey brain: I. *In vitro* autoradiography with [<sup>3</sup>H]CFT. *Synapse* **9**, 177–187 (1991).
- Dawson, T. M., Gehlert, D. R., McCabe, R. T., Barnett, A. & Wamsley, J. K. D1 dopamine receptors in the rat brain: a quantitative autoradiographic analysis. *J. Neurosci.* **6**, 2352–2365 (1986).
- Mansour, A. *et al.* Localization of dopamine D2 receptor mRNA and D1 and D2 receptor binding in the rat brain and pituitary: an *in situ* hybridization-receptor autoradiographic analysis. *J. Neurosci.* **10**, 2587–2600 (1990).
- Memo, M. *et al.* Dopaminergic inhibition of prolactin release and calcium influx induced by neurotensin in anterior pituitary is independent of cyclic AMP system. *J. Neurochem.* **47**, 1689–1695 (1986).
- Rheinhard, J. E., Smith, G. K. & Nichol, C. A. A rapid and sensitive assay for tyrosine-3-monooxygenase based upon the release of [<sup>3</sup>H]-H<sub>2</sub>O and adsorption of [<sup>3</sup>H]-tyrosine by charcoal. *Life Sci.* **39**, 2185–2189 (1986).
- Blaha, C. D. *et al.* Modulation of dopamine efflux in the nucleus accumbens after cholinergic stimulation of the ventral tegmental area in intact, pedunculo-pontine tegmental nucleus-lesioned, and laterodorsal tegmental nucleus-lesioned rats. *J. Neurosci.* **16**, 714–722 (1996).
- Calabresi, P., Lacey, M. G. & North, R. A. Nicotinic excitation of rat ventral tegmental neurones *in vitro* studies by intracellular recording. *Br. J. Pharmacol.* **98**, 135–140 (1989).
- Merlo Pich, E. *et al.* Common neural substrates for the addictive properties of nicotine and cocaine. *Science* **275**, 83–86 (1997).
- Grahame, N. J., Phillips, T. J., Burkhart-Kasch, S. & Cunningham, C. L. Intravenous cocaine self-administration in the C57BL/6J mouse. *Pharmacol. Biochem. Behav.* **51**, 827–834 (1995).
- Tessari, M., Valerio, E., Chiamulera, C. & Beardsley, P. M. Nicotine reinforcement in rats with histories of cocaine self-administration. *Psychopharmacology* **121**, 282–283 (1995).
- McGehee, D. S., Heath, M. J., Gelber, S., Devay, P. & Role, L. W. Nicotine enhancement of fast excitatory synaptic transmission in CNS by presynaptic receptors. *Science* **269**, 1692–1696 (1995).
- Rimondini, R. *et al.* PEC-60 increases dopamine but not GABA release in the dorsolateral neostriatum of the halothane anaesthetized rat. An *in vivo* microdialysis study. *Neurosci. Lett.* **177**, 53–57 (1994).

**Supplementary information** is available on Nature's World-Wide Web site (<http://www.nature.com>) or as paper copy from Mary Sheehan at the London editorial office of Nature.

**Acknowledgements.** We thank M. Memo and D. Uberti for help and advice with DA-stimulated cyclase assays; M. Epping-Jordan for help with self-administration experiments; P. Sattouet-Roché for technical assistance; L. Gold, F. Caine and C. Chiamulera for discussing the behavioural results; and E. Ratti, D. Trist and A. North (GlaxoWellcome) for supporting part of the project. This work was supported by the Collège de France, the Centre National de la Recherche Scientifique, the Association Française contre la Myopathie, the Council for Tobacco Research, Biomed and Biotech contract from the Commission of the European Communities, a grant from the Human Frontiers Science Program, a Roux grant from the Institut Pasteur for C.L., a young investigator award from NARSAD and a grant from NIDA to M.R.P.

Correspondence and requests for materials should be addressed to J.P.C.

## Extreme Th1 bias of invariant V $\alpha$ 24J $\alpha$ Q T cells in type 1 diabetes

S. Brian Wilson<sup>†</sup>, Sally C. Kent<sup>†</sup>, Kurt T. Patton<sup>‡</sup>,  
Tihamer Orban<sup>§</sup>, Richard A. Jackson<sup>§</sup>, Mark Exley<sup>||</sup>,  
Steven Porcell<sup>||</sup>, Desmond A. Schatz<sup>#</sup>, Mark A. Atkinson<sup>#</sup>,  
Steven P. Balk<sup>||</sup>, Jack L. Strominger<sup>\*</sup> & David A. Hafler<sup>‡</sup>

<sup>\*</sup> Department of Molecular and Cellular Biology, Harvard University, Cambridge, Massachusetts 02138, USA

<sup>‡</sup> Center for Neurologic Diseases, Brigham and Women's Hospital; <sup>§</sup> Immunology Section, Joslin Diabetes Center; <sup>||</sup> Cancer Biology Program, Hematology/Oncology Division, Beth Israel Deaconess Medical Center; <sup>¶</sup> Lymphocyte Biology Section, Division of Rheumatology, Immunology and Allergy, Brigham and Women's Hospital; Harvard Medical School, Boston, Massachusetts 02115, USA

<sup>#</sup> Departments of Pathology and Pediatrics, University of Florida, Gainesville, Florida 32610, USA

<sup>†</sup> These authors contributed equally to this work.

Type 1 diabetes (insulin-dependent diabetes mellitus, IDDM) is a disease controlled by the major histocompatibility complex (MHC) which results from T-cell-mediated destruction of pancreatic  $\beta$ -cells<sup>1</sup>. The incomplete concordance in identical twins and the presence of autoreactive T cells and autoantibodies in individuals who do not develop diabetes suggest that other

abnormalities must occur in the immune system for disease to result<sup>2,3</sup>. We therefore investigated a series of at-risk non-progressors and type 1 diabetic patients (including five identical twin/triplet sets discordant for disease). The diabetic siblings had lower frequencies of CD4<sup>+</sup>CD8<sup>−</sup> Vα24JαQ<sup>+</sup> T cells compared with their non-diabetic sibling. All 56 Vα24JαQ<sup>+</sup> clones isolated from the diabetic twins/triplets secreted only interferon (IFN)-γ upon stimulation; in contrast, 76 of 79 clones from the at-risk non-progressors and normals secreted both interleukin (IL)-4 and IFN-γ. Half of the at-risk non-progressors had high serum levels of IL-4 and IFN-γ. These results support a model for IDDM in which Th1-cell-mediated tissue damage is initially regulated by Vα24JαQ<sup>+</sup> T cells producing both cytokines; the loss of their capacity to secrete IL-4 is correlated with IDDM.

The discovery of Th1 and Th2 subsets of CD4<sup>+</sup> T cells has helped to explain the cellular basis for the diversity of T-cell responses in autoimmunity<sup>4</sup>. Th1 cells promote inflammatory cellular immune responses and are biased towards secretion of IFN-γ, tumour-necrosis factor (TNF)-β and IL-2. Th2 cells are biased towards secretion of interleukins 4, 5, 6, 10 and 13, induce humoral immunity, and inhibit Th1 responses. Lymphocyte cytokine production in type 1 diabetes is known to exhibit a bias towards the Th1 cytokine IFN-γ (ref. 5), but the cellular mechanisms integrating the drive to Th1 or Th2 effector cell differentiation are poorly understood. In the mouse, one mechanism by which Th2 rather than Th1 T-cell bias may be promoted is by activation of invariant (no N/P nucleotide additions within the CDR3 of the *TCRA* gene) Vα14Jα281 TCR<sup>+</sup> NK 1.1<sup>+</sup> T cells capable of early secretory bursts of IL-4 and IFN-γ. The ligand for this family of T cells is CD1.1 on the surface of antigen-presenting cells<sup>6,7</sup>.

CD4<sup>+</sup>CD8<sup>−</sup> T cells in humans expressing the invariant Vα24JαQ T-cell antigen receptor (TCR) which has close sequence homology to the murine Vα14Jα281 TCR have been described<sup>8</sup>. To determine whether there could be a relationship between the number of circulating CD4<sup>+</sup>CD8<sup>−</sup> Vα24JαQ<sup>+</sup> T cells and type 1 diabetes, we did a frequency analysis on a set of type 1 diabetic discordant monozygotic twins and triplets. The numbers of circulating CD4<sup>+</sup>CD8<sup>−</sup> Vα24JαQ<sup>+</sup> T cells in diabetes-free twins/triplets were compared with those present in their siblings with disease. The percentage of circulating invariant CD4<sup>+</sup>CD8<sup>−</sup> Vα24JαQ T cells could be determined by multiplying the frequency of invariant Vα24JαQ sequences present in the total CD4<sup>+</sup>CD8<sup>−</sup> Vα24<sup>+</sup> population by the percentage of CD4<sup>+</sup>CD8<sup>−</sup> Vα24<sup>+</sup> T cells, as measured by flow cytometric analysis (Table 1). No CD4<sup>+</sup>CD8<sup>−</sup> Vα24JαQ<sup>+</sup> T cells were detected in three diabetics, despite at least three sorting attempts for each subject. The percentage of CD4<sup>+</sup>CD8<sup>−</sup> Vα24JαQ<sup>+</sup> T cells in a previously disease-free diabetic twin (patient 6A; Table 1), studied during the week of IDDM diagnosis, was similar to that in the long-term IDDM twin and in the other diabetics. In all sets of family pairings, the IDDM sibling had markedly lower percentages of CD4<sup>+</sup>CD8<sup>−</sup> Vα24JαQ<sup>+</sup> T cells ( $P = 0.015$ , paired sign test using only the discordant twins/triplets data).

To determine whether human Vα24JαQ<sup>+</sup> T cells were functionally altered in type 1 diabetics and those at risk for the disease, single CD4<sup>+</sup>/CD8<sup>−</sup> mononuclear cells expressing Vα24<sup>+</sup> TCR were cloned. The initial analysis was carried out on clones generated from the IDDM non-progressing member of a sibling pair, subject 7A (Table 1). All clones expressed the invariant Vα24JαQ junctional sequences conserving the germ-line-encoded amino acids Vα24 (-CVVS-) and JαQ (:DRGST-). Eight of ten clones were Vβ11<sup>+</sup> and two were Vβ13<sup>+</sup>. All of the clones were CD4<sup>+</sup> and uniformly negative when stained for CD8 β-chain. Surface expression of CD8α<sup>+</sup> appeared to reflect the activation state, as staining for this marker reverted to negative 2–3 weeks post-stimulation. All T-cell clones expressed the human homologue of the murine NK1.1 molecule, NKR-P1A (ref. 9), and the C-type lectins encoded by the natural killer (NK) locus, CD69 and CD94 (data not shown).

CD1d restriction was assessed by co-cultivating Vα24JαQ<sup>+</sup> T-cell clones with C1R cells transfected with a CD1d or control expression vector<sup>10</sup>. A T-cell clone (4.2) with a non-invariant TCR α-chain (Vα24N3Jα6) was included as a negative control. All T-cell clones, except 3.5, 3.8 and the control clone 4.2, specifically proliferated in response to the CD1d transfectant of C1R (Fig. 1a). All of the clones except 3.5 and 4.2 secreted IL-4 and IFN-γ in a CD1d-specific manner (Fig. 1b, c). Clone 3.5 secreted only IFN-γ in response to CD1d (Fig. 1). The fine specificity of the clones for CD1d was tested by using C1R targets transfected with CD1a, CD1c, CD1d or vector alone. Only CD1d-expressing target cells specifically stimulated each of the CD4<sup>+</sup>CD8<sup>−</sup> Vα24JαQ<sup>+</sup> clones, as assessed by IL-4 and IFN-γ secretion (Fig. 2).

A panel of Vα24JαQ<sup>+</sup> T-cell clones was then raised from: (1) the twins/triplets discordant for type 1 diabetes (Table 1); (2) from an additional four at-risk non-progressors with raised serum IL-4 levels (see below); and (3) two haplotype (DR3/DR2 and DR4/DRX)-matched normal controls. Twenty-five out of 28 clones raised from the at-risk non-progressors among the discordant twins/triplets secreted both IL-4 and IFN-γ (>10 pg ml<sup>−1</sup>) on stimulation with anti-CD3 (Fig. 3a). The other three clones produced only IFN-γ. Unlike the other non-progressing twins, only one clone from triplet 1A secreted moderate amounts of IL-4 when stimulated. Only a single attempt to generate clones from this subject was made owing to subsequent entry into a clinical trial. All of the 56 clones raised from the diabetic twins/triplets secreted only IFN-γ with anti-CD3 stimulation, and diabetic twins 4B and 5B had no identifiable CD4<sup>+</sup>CD8<sup>−</sup> Vα24JαQ<sup>+</sup> T cells (Table 1). There was no difference in the proliferative response to anti-CD3 between the clones raised from diabetics or other subjects (data not shown). The new onset type 1 twin 6A (Table 1) had 9/9 CD4<sup>+</sup>CD8<sup>−</sup> Vα24JαQ<sup>+</sup> T-cell clones that secreted only IFN-γ (Fig. 3b). This suggested that the Th1 phenotype seen in the new-onset twin was not related to duration of diabetes but occurred before, or concurrently with, the

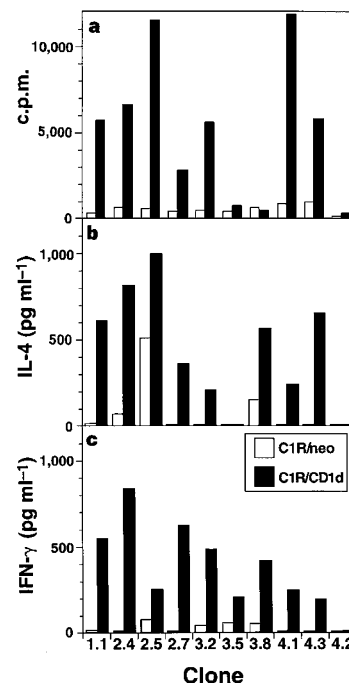


**Figure 1** CD4<sup>+</sup>CD8<sup>−</sup> Vα24JαQ T-cell clones respond to C1R/CD1d transfectants specifically. Vα24JαQ T cell clones (1.1, 2.4, 2.5, 2.7, 3.2, 3.5, 3.8, 4.1 and 4.3) and control clone 4.2 (Vα24N3Jα6), all at  $5 \times 10^4$  per well, were stimulated with fixed C1R/CD1d or C1R/neo transfected cells at  $5 \times 10^4$  per well. PMA (1 ng ml<sup>−1</sup>) was added. **a**, Proliferation was measured by tritiated thymidine incorporation at 72 h; **b**, secreted IL-4, and **c**, IFN-γ were assayed by ELISA at 48 h. All clones were from subject 7A. One of three representative experiments is shown.

onset of overt disease. As individuals discordant for the development of type 1 diabetes were genetically identical, the question remains as to what environmental factor(s), if any, may have triggered the decreased frequency and cytokine shift of the V $\alpha$ 24J $\alpha$ Q T cells.

An additional set of 33 clones was generated from four at-risk non-progressors (see below and Fig. 4), and 18 clones were raised from MHC haplotype-matched controls (Fig. 3b). Clones raised from these subjects were phenotypically similar to the diabetes-free twins and a series of invariant V $\alpha$ 24J $\alpha$ Q<sup>+</sup> T-cell clones previously described<sup>10,11</sup>. Thus, all V $\alpha$ 24J $\alpha$ Q T-cell clones raised from type 1 patients showed an extreme Th1 bias, making them incapable of providing the IL-4 necessary for initiation of Th2 responses. In fact,

unopposed IFN- $\gamma$  secretion could augment or initiate a Th1-dominated cellular attack on pancreatic  $\beta$ -cells<sup>12,13</sup>.

Our functional studies on V $\alpha$ 24J $\alpha$ Q<sup>+</sup> T cells from discordant twins/triplets, at-risk non-progressors and controls suggested that these two groups had polarized cell-mediated immune responses. We therefore tested serum IL-4 and IFN- $\gamma$  in 14 at-risk IDDM non-progressors who had remained IDDM-free despite a 50% risk of developing diabetes during the study<sup>14</sup>. This cohort was defined by having remained healthy despite five or more years follow-up after diagnosis of type 1 diabetes in a first-degree relative and being positive for islet-cell antibodies (ICA<sup>+</sup>) with any two of the following autoantibodies: anti-GAD, anti-IA2 or anti-insulin autoantibodies. Seven of 14 type 1 non-progressors had markedly raised levels of serum IL-4 (Fig. 4), six of whom also had raised IFN- $\gamma$  (0.2–35 ng ml<sup>-1</sup>). Despite the increase in cytokines in the serum from

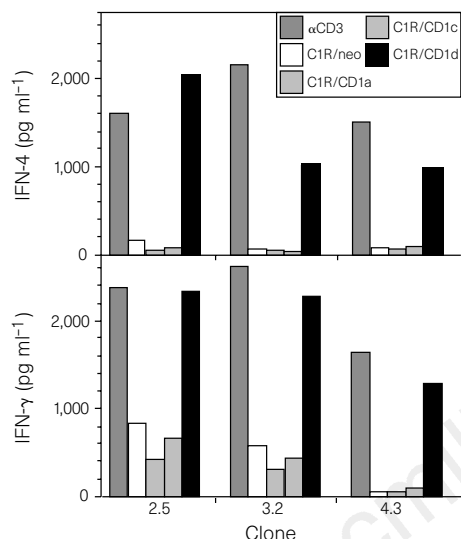


**Figure 2** Specificity of three CD4<sup>+</sup>CD8<sup>-</sup> V $\alpha$ 24J $\alpha$ Q T-cell clones for CD1 isoforms. Clones 2.5, 3.2 and 4.3 were co-cultivated with the following C1R transfectants: C1R/neo, C1R/CD1a, C1R/CD1c, and C1R/CD1d, as for Fig. 1: top, secreted IL-4; bottom, secreted IFN- $\gamma$ . In addition, clones were activated with plate-bound anti-CD3 or immunoglobulin control.

**Table 1** Frequency of CD4<sup>+</sup>CD8<sup>-</sup> V $\alpha$ 24J $\alpha$ Q T cells from IDDM and disease-free siblings

Twins/triplets	DN (%) <sup>*</sup>	% DN V $\alpha$ 24 <sup>+</sup> in total lymphocytes	V $\alpha$ 24J $\alpha$ Q DN sequence frequency	V $\alpha$ 24J $\alpha$ Q (%)
1A/IL-4 <sup>+</sup>	0.74	0.04	20/22	0.036
1B/IDDM	0.95	0.01	10/19	0.005
1C/IDDM	0.76	0.04	9/22	0.016
2A	2.1	0.37	9/10	0.33
2B/IDDM	3.1	0.025	31/31	0.025
3A	1.1	0.04	8/12	0.027
3B/IDDM	1.89	0.01	5/15	0.003
4A	1.21	0.02	4/13	0.006
4B/IDDM	0.31	0.006	0†	0
5A	0.58	0.06	8/12	0.04
5B/IDDM	0.98	0	0†	0
6A/new IDDM	0.89	0.03	7/26	0.008
6B/IDDM	2.62	0.03	8/23	0.01
Brother/sister				
7A/IL-4 <sup>+</sup>	2.54	0.03	8/12	0.017
7B/IDDM	1.08	0.005	0/18	0

The frequency of V $\alpha$ 24J $\alpha$ Q TCR sequences was determined by sorting all CD4<sup>+</sup>CD8<sup>-</sup>  $\alpha$ TCR<sup>+</sup> T cells, amplifying all V $\alpha$ 24 transcripts and sequencing the TCR CDR3 region; the percentage of cells that were invariant CD4<sup>+</sup>CD8<sup>-</sup> V $\alpha$ 24J $\alpha$ Q in total mononuclear cells was calculated by multiplying the sequence frequency by the CD4<sup>+</sup>CD8<sup>-</sup> V $\alpha$ 24<sup>+</sup> percentage of total mononuclear cells, as determined by flow cytometry. IL-4<sup>+</sup> indicates a subject with high serum IL-4. <sup>\*</sup> DN, CD4<sup>+</sup>CD8<sup>-</sup>. <sup>†</sup> No V $\alpha$ 24 PCR products were detected in three attempts.

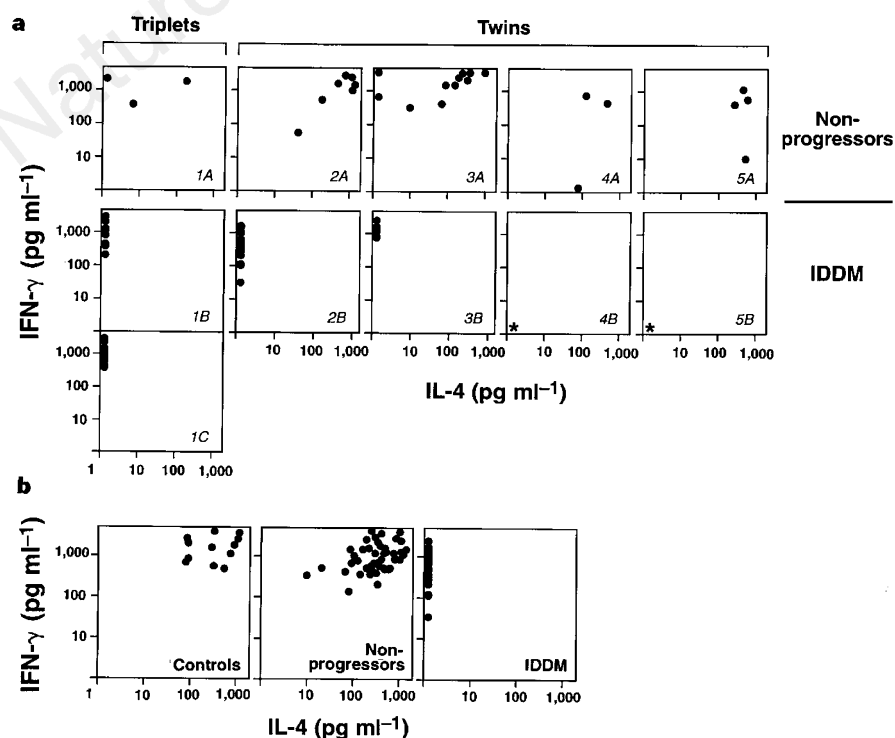


**Figure 3** IL-4 and IFN- $\gamma$  secretion profiles of CD4<sup>+</sup>CD8<sup>-</sup> V $\alpha$ 24J $\alpha$ Q T-cell clones raised from monozygotic twins and triplets discordant for IDDM. **a**, Plate-bound anti-CD3 or control immunoglobulin was used to stimulate individual clones and secreted IL-4 and IFN- $\gamma$  was assayed at 4 h. The pattern of cytokine secretion was similar at 24 h. The CDR3 T-cell receptor sequences were determined and the surface phenotype was confirmed by flow cytometry for every clone (data not shown). Asterisks, twins with IDDM (4B and 5B) had no detectable V $\alpha$ 24J $\alpha$ Q T cells in two attempts to sort from 20 million PBMCs (Table 1). **b**, CD4<sup>+</sup>CD8<sup>-</sup> V $\alpha$ 24J $\alpha$ Q T-cell clones from 4 IDDM non-progressing subjects (Fig. 4), two control (DR2/DR3 and DR4/DRX) and five IDDM patients (triplets 1B and 1C, twins 2B and 3B, and new-onset IDDM twin 6A), were assayed as described in **a**.

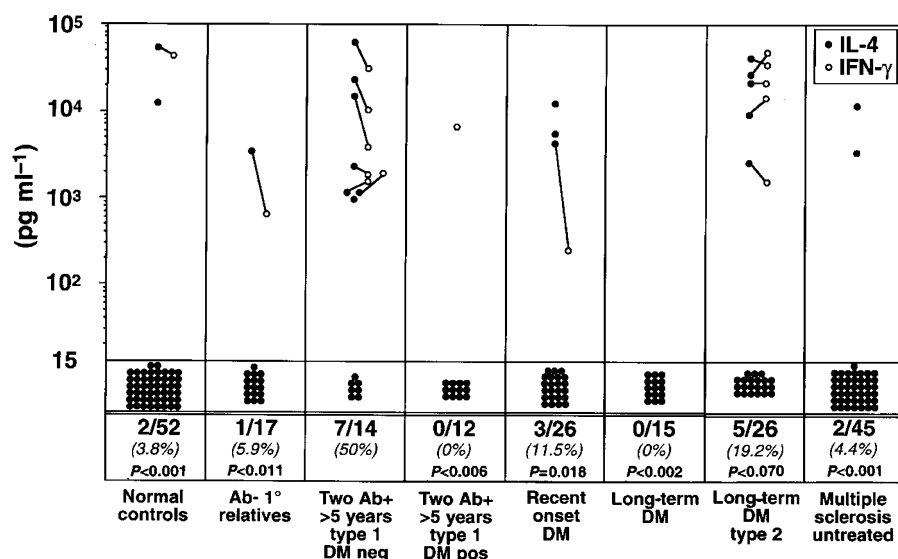


**Figure 4** Serum IL-4 and IFN- $\gamma$  in type 1 diabetes. Sera were collected and assayed for IL-4 and IFN- $\gamma$  by capture ELISA, the detection minimum for which was 15 pg ml<sup>-1</sup>. Raised cytokines were detected in 7/14 members of the at-risk IDDM non-progressor cohort. Lines connecting symbols indicate samples in which both IL-4 and IFN- $\gamma$  were detected; no IFN- $\gamma$  was detected in six subjects with raised IL-4. \**P*, Two-tailed Fisher exact test comparing high IL-4 frequency in each cohort with at-risk IDDM non-progressors.

seven of fourteen non-progressors, all seven IL-4<sup>+</sup> individuals have remained healthy with no evidence of chronic infectious or atopic/allergic illnesses. Both cytokines in the remaining seven were below the detection limit of our enzyme-linked immunosorbent assay (ELISA; 0.015 ng ml<sup>-1</sup>). Five of 14 individuals in this group were found to have the strongly protective MHC allele DQB1\*0602 and therefore are not at the same risk of progression as the remaining nine members of this cohort<sup>15</sup>. Three of these five individuals had raised serum IL-4 and IFN- $\gamma$  levels, in contrast to our finding that IL-4 was undetectable in the serum (before or after diagnosis of type 1 diabetes) in 12 individuals with identical autoantibody status who developed IDDM after five or more years of follow up (Fig. 4).

Raised cytokines were also detected in archival serum samples obtained from 3/23 individuals at the time of diagnosis of type 1 diabetes and in 5/26 type-2 diabetics who did not have autoantibodies or a family history of type 1 diabetes (Fig. 4). When compared with normals, antibody-positive first-degree relatives, recent-onset diabetics, long-term diabetics (IDDM >2 years), autoantibody-negative first-degree relatives or untreated patients with multiple sclerosis (MS), the frequency of serum IL-4<sup>+</sup> individuals was significantly raised in the non-progressor consort (Fig. 4). The authenticity of the IL-4 detected was confirmed independently by using another set of ELISA antibodies, by binding to soluble recombinant IL-4 receptor produced in insect cells, and by western blot (data not shown).

Our results demonstrate a relationship between elevated serum IL-4 levels and resistance to the progression of an autoimmune disorder. Prolonged hyperglycaemia as an explanation for the absence of IL-4 in type 1 diabetics is less likely because IL-4 was detected in the serum of type 2 diabetics. Increased IL-4 was not an absolute predictor of IDDM resistance as only half of the resistant cohort had raised serum IL-4, as did 3/23 diabetics at or near the time of diagnosis.

In the non-obese diabetic (NOD) mouse, there is evidence that IL-4 exerts a dominant-negative effect on the progression to IDDM<sup>16–18</sup>. Differentiation of T cells into IL-4 secreting Th2 effector cells requires IL-4 priming<sup>4</sup>. Although this proposed function for NK1.1<sup>+</sup> T cells was not obligatory for all Th2 immune responses<sup>6,19,20</sup>, T-cell IL-4 secretion was markedly diminished in a CD1 knockout background<sup>20–22</sup>. Fewer NK 1.1<sup>+</sup> T cells were found to be present and were less frequent before the onset of disease in several murine methods of autoimmunity<sup>6,7,23–25</sup>. In these models, autoimmunity was accelerated by depletion of NK 1.1<sup>+</sup> T cells and delayed by generating mice transgenic for the V $\alpha$ 24J $\alpha$ 281 TCR. Diabetes was also prevented in the NOD mouse by adoptive transfer of a population harbouring the NK1.1-like class of T cell<sup>26</sup>.

In summary, type 1 diabetes is associated with an extreme Th1 phenotype for V $\alpha$ 24J $\alpha$ Q<sup>+</sup> T cells and a decrease in their circulating frequency. Our results suggest that there is a strong link between V $\alpha$ 24J $\alpha$ Q<sup>+</sup> T cells and human type 1 diabetes; this indicates that they may be functionally related to the resistance or progression of this autoimmune disease in humans. □

## Methods

**Antibodies and phenotypic analysis of T cells.** Flow cytometry experiments were done on FACScaliber and FACS Vantage instruments (Becton Dickinson). Monoclonal antibody (mAb) DX1 was a gift from L. Lanier; anti-CD4, anti-CD8 and anti-panTCR were from Becton Dickinson; anti-V $\alpha$ 24, anti-CD8 $\beta$ , anti-CD56, anti-CD16 and anti-p58CD158 (NK workshop mAbs GL183 and EB6) were from Immunotech; anti-CD69 and anti-CD94 were from Pharmingen.

**CDR3 TCR sequencing.** Total CD4<sup>+</sup>CD8<sup>+</sup> V $\alpha$ 24J $\alpha$ Q CDR3 sequences were amplified by reverse transcription followed by polymerase chain reaction (RT-PCR) using V $\alpha$ 24 and constant-region-specific primers as described<sup>8</sup>, and cloned using a Stratagene pCR-Script kit. Individual T-cell clones TCR transcripts were amplified by RT-PCR. Sequences of the plasmid and PCR DNA products were determined directly on an ABI 373A Automated DNA Sequencer.

**Cell culture and cytokine assay.** Single-cell sorts were grown with a mixture of irradiated (5,000 rad) allogeneic feeders at 50,000 per well and 721.221 cells at 5,000 per well and supplemented with 1  $\mu$ g ml<sup>-1</sup> PHA-P, IL-2 and IL-7 each at 10 U ml<sup>-1</sup>, then propagated as described<sup>27</sup>. Clones positive for V $\alpha$ 24 and NKR-P1A by flow cytometry and a V $\alpha$ 24J $\alpha$ Q CDR3 TCR sequence were assayed for cytokine secretion. Cells were stimulated (25,000 per well) with plate-bound anti-CD3 (1  $\mu$ g ml<sup>-1</sup>; Immunotech) or control isotype antibody (Sigma) for 4, 8 or 24 h. Supernatants were assayed for IL-4 and IFN- $\gamma$  by capture ELISA, and after 24 h, 1  $\mu$ Ci per well of [<sup>3</sup>H]thymidine was added and incorporation measured as described<sup>27</sup>.

**CD1 restriction.** Restriction experiments using CD1 isoform (CD1a, CD1c, CD1d and pSR $\alpha$ -neo vector alone) transfected C1R cells were done as described<sup>10</sup>.

Received 11 June; accepted 17 September 1997.

1. Davies, J. L. *et al.* A genome-wide search for human type-1 diabetes susceptibility genes. *Nature* **371**, 130–136 (1994).
2. Verge, C. F. *et al.* Late progression to diabetes and evidence for chronic  $\beta$ -cell autoimmunity in identical twins of patients with type 1 diabetes. *Diabetes* **44**, 1176–1179 (1995).
3. Roep, B. O. T cell responses to autoantigens in IDDM. The search for the holy grail. *Diabetes* **45**, 1147–1156 (1996).
4. Abbas, A. K., Murphy, K. M. & Sher, A., Functional diversity of helper T lymphocytes. *Nature* **383**, 787–793 (1996).
5. Kallmann, B. A. *et al.* Systematic bias of cytokine production toward cell-mediated immune regulation in IDDM and toward humoral immunity in Graves' disease. *Diabetes* **46**, 237–243 (1997).
6. Bendelac, A., Rivera, M. N., Park, H.-S. & Roark, J. H. Mouse CD1-specific NK1 T cells: development, specificity, and function. *Annu. Rev. Immunol.* **15**, 535–562 (1997).
7. Vicari, A. P. & Zlotnik, A. Mouse NK1.1<sup>+</sup> T cells: a new family of T cells. *Immunol. Today* **17**, 71–76 (1996).



8. Porcelli, S., Yockey, C. E., Brenner, M. B. & Balk, S. P. Analysis of T cell antigen receptor (TCR) expression by human peripheral blood CD4<sup>+</sup> 8<sup>+</sup> α/β T cells demonstrates preferential use of several Vβ genes and an invariant TCR α chain. *J. Exp. Med.* **178**, 1–16 (1993).
9. Lanier, L. L., Chang, C. & Phillips, J. H. Human NKR-P1A. A disulfide-linked homodimer of the C-type lectin superfamily expressed by a subset of NK and T lymphocytes. *J. Immunol.* **153**, 2417–2428 (1994).
10. Exley, M., Garcia, J., Balk, S. P. & Porcelli, S. Requirements for CD1d recognition by human invariant Va24<sup>+</sup> CD4<sup>+</sup>CD8<sup>+</sup> T cells. *J. Exp. Med.* **186**, 1–11 (1997).
11. Davodeau, F. *et al.* Close phenotypic and functional similarities between human and murine αβ cells expressing invariant TCR α-chains. *J. Immunol.* **158**, 5603–5611 (1997).
12. von Herrath, M. G. & Oldstone, M. B. A. Interferon-γ is essential for destruction of β cells and development of insulin-dependent diabetes mellitus. *J. Exp. Med.* **185**, 531–539 (1997).
13. Denkers, E. Y., Scharton-Kersten, T., Barbieri, S., Caspar, P. & Sher, A. A role for CD4<sup>+</sup>NK1.1<sup>+</sup> T lymphocytes as major histocompatibility complex class II independent helper cells in the generation of CD8<sup>+</sup> effector function against intracellular infection. *J. Exp. Med.* **184**, 131–139 (1996).
14. Verge, C. F. *et al.* Prediction of type 1 diabetes in first-degree relatives using a combination of insulin, GAD, and ICA512bdc/IA-2 autoantibodies. *Diabetes* **45**, 926–933 (1996).
15. Pugliese, A. *et al.* HLA-DQB1\*0602 is associated with dominant protection from diabetes even among islet cell antibody-positive first-degree relatives of patients with IDDM. *Diabetes* **44**, 608–613 (1995).
16. Rapoport, M. J. *et al.* Interleukin 4 reverses T cell proliferative unresponsiveness and prevents the onset of diabetes in nonobese diabetic mice. *J. Exp. Med.* **178**, 87–99 (1993).
17. Mueller, R., Krahl, T. & Sarvetnick, N. Pancreatic expression of interleukin-4 abrogates insulinitis and autoimmune diabetes in nonobese diabetic (NOD) mice. *J. Exp. Med.* **184**, 1093–1099 (1996).
18. Fox, C. J. & Danska, J. S. IL-4 expression at the onset of islet inflammation predicts nondestructive insulinitis in nonobese diabetic mice. *J. Immunol.* **158**, 2414–2424 (1997).
19. Brown, D. R. *et al.* B2-microglobulin-dependent NK1.1<sup>+</sup> T cells are not essential for T helper cell 2 immune responses. *J. Exp. Med.* **184**, 1295–1304 (1996).
20. Smiley, S. T., Kaplan, M. H. & Grusby, M. J. Immunoglobulin E production in the absence of interleukin-4-secreting CD1-dependent cells. *Science* **275**, 977–979 (1997).
21. Chen, Y.-H., Chiu, N. M., Mandal, M., Wang, N. & Wang, C.-R. Impaired NK1<sup>+</sup> T cell development and early IL-4 production in CD1-deficient mice. *Immunity* **6**, 459–467 (1997).
22. Mendiratta, S. K. *et al.* CD1d1 mutant mice are deficient in natural T cells that promptly produce IL-4. *Immunity* **6**, 469–477 (1997).
23. Takeda, K. & Dennert, G. The development of autoimmunity in C57BL/6 *lpr* mice correlates with the disappearance of natural killer type 1-positive cells: evidence for their suppressive action on bone marrow stem cell proliferation, B cell immunoglobulin secretion, and autoimmune symptoms. *J. Exp. Med.* **177**, 155–164 (1993).
24. Mieza, M. A. *et al.* Selective reduction of Vα14<sup>+</sup> NK T cells associated with disease development in autoimmune-prone mice. *J. Immunol.* **156**, 4035–4040 (1996).
25. Gombert, J.-M. *et al.* IL-7 reverses NK1<sup>+</sup> T cell-defective IL-4 production in the non-obese diabetic mouse. *Int. Immunol.* **8**, 1751–1758 (1996).
26. Baxter, A. G., Kinder, S. J., Hammond, K. J. L., Scollay, R. & Godfrey, D. I. Association between αβTCR<sup>+</sup>CD4<sup>+</sup>CD8<sup>+</sup> T cell deficiency and IDDM in NOD/Lt mice. *Diabetes* **46**, 572–582 (1997).
27. Fukaura, H. *et al.* Induction of circulating myelin basic protein and proteolipid-specific transforming growth factor-β-secreting Th3 cells by oral administration of myelin in multiple sclerosis patients. *J. Clin. Invest.* **98**, 70–77 (1996).

**Acknowledgements.** We thank the DFCI flow cytometry facility for cell sorting, T. Smith for patient support, J. Orov for statistical analysis and A. LaMotte for clerical support. We wish to specifically thank the patients for their generosity without which these studies could not have been performed. These studies were supported by grants from the NIAID of the NIH.

Correspondence and requests for materials should be addressed to D.A.H.

## *Drosophila* Shaking-B protein forms gap junctions in paired *Xenopus* oocytes

Pauline Phelan, Lucy A. Stebbings, Richard A. Baines†, Jonathan P. Bacon, Jane A. Davies & Chris Ford\*

Sussex Centre for Neuroscience and \*Department of Genetics and Development, School of Biological Sciences, University of Sussex, Brighton BN1 9QG, UK

In most multicellular organisms direct cell–cell communication is mediated by the intercellular channels of gap junctions. These channels allow the exchange of ions and molecules that are believed to be essential for cell signalling during development and in some differentiated tissues. Proteins called connexins, which are products of a multigene family, are the structural components of vertebrate gap junctions<sup>1,2</sup>. Surprisingly, molecular homologues of the connexins have not been described in any invertebrate. A separate gene family, which includes the *Drosophila* genes *shaking-B* and *l(1)ogre*, and the *Caenorhabditis elegans* genes *unc-7* and *eat-5*, encodes transmembrane proteins with a predicted structure similar to that of the connexins<sup>3–9</sup>. *shaking-B* and *eat-5* are required for the formation of functional gap junctions<sup>8,10</sup>. To test directly whether Shaking-B is a channel protein, we expressed

it in paired *Xenopus* oocytes. Here we show that Shaking-B localizes to the membrane, and that its presence induces the formation of functional intercellular channels. To our knowledge, this is the first structural component of an invertebrate gap junction to be characterized.

The *shaking-B* (*shak-B*) locus was identified in *Drosophila* in two independent screens for behavioural mutants<sup>11,12</sup>. Two transcripts, referred to as *shak-B(neural)* (formerly *Passover*) and *shak-B(lethal)*, which share five 3' exons, encode proteins of relative molecular mass 43,000 to 44,000 (*M<sub>r</sub>* 43K–44K)<sup>3–5</sup>. Both are predicted to have four transmembrane domains, two extracellular loops, and cytoplasmic amino and carboxy termini<sup>3</sup>. By comparing dye-coupling in wild-type and mutant flies, we have shown that the product of *shak-B(neural)* is essential for the function of the gap junctions at electrical synapses in the giant fibre system, the pathway that subserves the insect's escape response<sup>10</sup>, and in some embryonic somatic muscle (R.A.B. *et al.*, unpublished data). These studies in *Drosophila* do not tell us whether Shak-B proteins are integral channel components of gap junctions or accessory proteins necessary for gap junctions to function. To distinguish between these possibilities we expressed *shak-B* RNAs in the *Xenopus* oocyte system, which has been used extensively to characterize the channel-forming ability of the vertebrate connexins<sup>13</sup>.

RNAs encoding Shak-B(neural) and Shak-B(lethal) were micro-injected, either individually or together, into the vegetal hemisphere of single oocytes. We first checked whether the oocytes efficiently

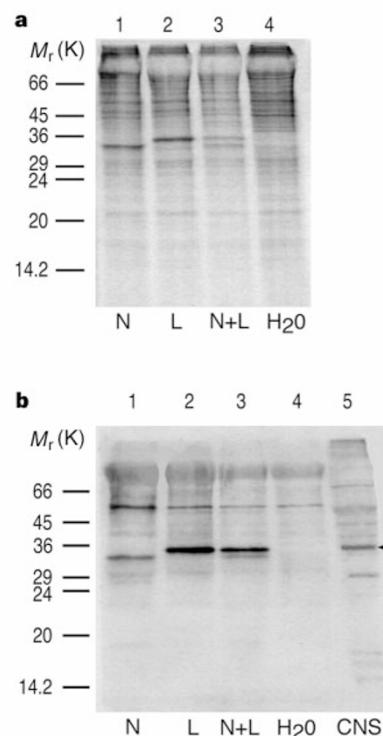


**Figure 1** *shak-B* RNA is translated in the *Xenopus* oocyte expression system. **a**, Total radiolabelled proteins in membranes (single cell equivalent) prepared from oocytes 24 h after injection of [<sup>35</sup>S] methionine (0.3 μCi) and 10 ng of *shak-B(neural)* RNA (N, lane 1), *shak-B(lethal)* RNA (L, lane 2), both RNAs (N + L, lane 3), or water (H<sub>2</sub>O, lane 4). Bands unique to the RNA-injected cells (lanes 1–3) are Shak-B proteins. **b**, Western blot of proteins in membranes (half-cell equivalent) of RNA or water-injected oocytes (lanes 1–4, as in **a**) and in a homogenate of adult *Drosophila* nervous systems (CNS, lane 5). The blot was probed with Shak-B antiserum<sup>10</sup>. Labelled proteins (lanes 1–3) correspond in size to the proteins uniquely detected in **a** (lanes 1–3), and to native *Drosophila* Shak-B protein (lane 5, arrowhead). Positions of *M<sub>r</sub>* markers are indicated on the left.

† Present address: Zoology Department, University of Cambridge, Cambridge CB2 3EJ, UK.

responsible for ocular-dominance plasticity, why is there ever any shift in ocular dominance after monocular inactivation? There are several possible reasons why plasticity can be observed with prolonged monocular inactivation in younger animals. First, some level of noise almost certainly converges on cortical neurons even after retinal TTX treatment. Monocular inactivation does not completely eliminate activity in the LGN afferents serving the deprived eye, and even spontaneous presynaptic release of glutamate can activate NMDA-receptor-mediated postsynaptic currents at some synapses<sup>22</sup>. It is possible that such weak presynaptic activity could cause synaptic depression, given enough time (especially in young animals, in which the mechanisms of LTD are highly expressed<sup>17,18</sup>). Second, because ocular dominance is a measurement of relative response magnitude, part of the shift could be accounted for by homosynaptic potentiation of the non-deprived afferents<sup>4</sup>. Finally, it is possible that the mechanisms of ocular-dominance plasticity are different in animals of less than five weeks in age.

The synaptic depression induced by visual deprivation is more pronounced when one eye is deprived (monocular deprivation) than when both eyes are deprived (binocular deprivation)<sup>23</sup>. This observation led to the early suggestion<sup>24,25</sup> that *heterosynaptic* LTD occurs in visual cortex (that is, a depression of inactive deprived-eye synapses that is triggered by the strong activation of the post-synaptic neuron by the non-deprived eye). The BCM theory offers an alternative explanation for the difference between the effects of monocular and binocular deprivation. According to this theory, the amount of homosynaptic depression induced by presynaptic activity varies depending on the average level of cortical activity, which is higher during monocular deprivation than during binocular deprivation<sup>4</sup>. Indeed, in agreement with the theory, it has been shown experimentally that homosynaptic LTD is significantly reduced in binocularly deprived cortex<sup>26</sup>.

The occurrence of homosynaptic depression may, therefore, be sufficient to account for the initial loss of cortical responsiveness to visual inputs to an eye that was deprived of normal vision for a period of time. If this hypothesis is correct, we could be on the threshold of unprecedented insight into the detailed molecular mechanisms of one form of visual cortical plasticity. □

## Methods

**Injection and lid suture.** Kittens were anaesthetized by continuous administration of isoflurane gas (2–3% in 100% O<sub>2</sub> at 1 l min<sup>-1</sup>). Ten animals received an injection of TTX (4 µl of 1.25 mM TTX in 5% citrate buffer; Calbiochem) into the vitreous humour of the left eye; ten others received an injection of 4 µl saline. Injections were performed without experimenter knowledge of the contents of the injection syringe; experimenters remained blind until the analysis of all experiments had been completed. Following the injection, the margins of the upper and lower lids of the injected eye were trimmed and sutured together. The entire procedure was completed in less than 20 min and the kittens then recovered rapidly. Previous work<sup>10</sup> and pilot studies in our laboratory indicated that the TTX inactivates the retina completely for two days, after which the retina recovers gradually over another two days.

**Electrophysiology and visual stimulation.** Animals were prepared for electrophysiology and visual stimulation as described<sup>27</sup>. Multiunit activity was recorded using glass-covered tungsten electrodes with an impedance of 0.8–1.5 MΩ. The visual stimulation used to quantify responses consisted of high-contrast, drifting sinusoidal gratings with a spatial frequency of 1 cycle per degree and a temporal frequency of 1 Hz. These stimulus parameters were chosen because, in our experience, they elicit a response from most cortical cells. The grating stimuli were 19° tall × 28° wide, and extended well beyond the receptive fields of both eyes. Gratings were presented at 16 different orientations/directions that varied by 22.5° around a full 360°. Each grating orientation/direction was presented 5 times for 5 s each. Data were also collected during 5 blank-screen trials (5 sec each) to measure spontaneous activity. To ensure that we did not oversample from the first ocular-dominance column, the electrode penetrations were highly oblique, beginning medial to the crown of the lateral gyrus and running parallel to the cortical surface, down

the medial wall of the hemisphere. The tracks were always long enough to sample complete ipsi-contra eye cycles of ocular dominance.

Received 27 October; accepted 1 December 1998.

1. Bienenstock, E. L., Cooper, L. N. & Munro, P. W. Theory for the development of neuron selectivity: orientation specificity and binocular interaction in visual cortex. *J. Neurosci.* **2**, 32–48 (1982).
2. Bear, M. F., Cooper, L. N. & Ebner, F. F. A physiological basis for a theory of synaptic modification. *Science* **237**, 42–48 (1987).
3. Bear, M. F. in *Mechanistic Relationships between Development and Learning* (eds Carew, T. J., Menzel, R. & Shatz, C. J.) 205–225 (Wiley, New York, 1998).
4. Blais, B. S., Shouval, H. Z. & Cooper, L. N. The role of presynaptic activity on the ocular dominance shift in monocular deprivation: comparison of homosynaptic and heterosynaptic mechanisms. *Proc. Natl Acad. Sci. USA* **96**, 1083–1087 (1999).
5. Greuel, J. M., Luhman, H. J. & Singer, W. Evidence for a threshold in experience-dependent long-term changes of kitten visual cortex. *Dev. Brain Res.* **34**, 141–149 (1987).
6. Chapman, B., Jacobson, M. D., Reiter, H. O. & Stryker, M. P. Ocular dominance shift in kitten visual cortex caused by imbalance in retinal electrical activity. *Nature* **324**, 154–156 (1986).
7. Mower, G. D. The effect of dark rearing on the time course of the critical period in cat visual cortex. *Dev. Brain Res.* **58**, 151–158 (1991).
8. Hubel, D. H. & Wiesel, T. N. The period of susceptibility of the physiological effects of unilateral eye closure in kittens. *J. Physiol.* **206**, 419–436 (1970).
9. Kaplan, E., Purpura, K. & Shapley, R. M. Contrast affects the transmission of visual information through the mammalian lateral geniculate nucleus. *J. Physiol. (Lond.)* **391**, 267–288 (1987).
10. Stryker, M. P. & Harris, W. A. Binocular impulse blockade prevents the formation of ocular dominance columns in cat visual cortex. *J. Neurosci.* **6**, 2117–2133 (1986).
11. Reiter, H. O. & Stryker, M. P. Neural plasticity without postsynaptic action potentials: less active inputs become dominant when kitten visual cortical cells are pharmacologically inhibited. *Proc. Natl Acad. Sci. USA* **85**, 3623–3627 (1988).
12. Bear, M. F., Kleinschmidt, A., Gu, Q. & Singer, W. Disruption of experience-dependent synaptic modifications in striate cortex by infusion of an NMDA receptor antagonist. *J. Neurosci.* **10**, 909–925 (1990).
13. Ramoa, A. S., Paradiso, M. A. & Freeman, R. D. Blockade of intracortical inhibition in the kitten striate cortex: effect on receptive field properties and associated loss of ocular dominance plasticity. *Exp. Brain Res.* **73**, 285–296 (1988).
14. Artola, A. & Singer, W. Long-term depression of excitatory synaptic transmission and its relationship to long-term potentiation. *Trends Neurosci.* **16**, 480–487 (1993).
15. Bear, M. F. & Kirkwood, A. in *Cortical Plasticity: LTP and LTD* (eds Fazili, M. S. & Collingridge, G. L.) 191–205 (Bios Scientific, Oxford, 1996).
16. Bear, M. F. & Singer, W. Modulation of visual cortical plasticity by acetylcholine and noradrenaline. *Nature* **320**, 172–176 (1986).
17. Dudek, S. M. & Friedlander, M. J. Developmental down-regulation of LTD in cortical layer IV and its independence of modulation by inhibition. *Neuron* **16**, 1–20 (1996).
18. Kirkwood, A., Silva, A. & Bear, M. F. Age-dependent decrease of synaptic plasticity in the neocortex of αCaMKII mutant mice. *Proc. Natl Acad. Sci. USA* **94**, 3380–3383 (1997).
19. Kirkwood, A. & Bear, M. F. Homosynaptic long-term depression in the visual cortex. *J. Neurosci.* **14**, 3404–3412 (1994).
20. Kojic, L., Gu, Q., Douglas, R. M. & Cynader, M. Serotonin facilitates synaptic plasticity in kitten visual cortex: an *in vitro* study. *Dev. Brain Res.* **101**, 299–304 (1997).
21. Kirkwood, A., Rozas, C., Kirkwood, J., Perez, F. & Bear, M. F. Modulation of long-term synaptic depression in visual cortex by acetylcholine and norepinephrine. *J. Neurosci.* (in the press).
22. Sah, P., Hestrin, S. & Nicoll, R. A. Tonic activation of NMDA receptors by ambient glutamate enhances excitability of neurons. *Science* **246**, 815–818 (1989).
23. Wiesel, T. N. & Hubel, D. H. Comparison of the effects of unilateral and bilateral eye closure on cortical unit responses in kittens. *J. Neurophysiol.* **28**, 1060–1072 (1965).
24. Stent, G. S. A physiological mechanism for Hebb's postulate of learning. *Proc. Natl Acad. Sci. USA* **70**, 997–1001 (1973).
25. von der Malsburg, C. Self-organization of orientation-sensitive columns in the striate cortex. *Kybernetik* **14**, 85–100 (1973).
26. Kirkwood, A., Rioult, M. G. & Bear, M. F. Experience-dependent modification of synaptic plasticity in visual cortex. *Nature* **381**, 526–528 (1996).
27. Rossi, A. F., Rittenhouse, C. D. & Paradiso, M. A. The representation of brightness in primary visual cortex. *Science* **273**, 1104–1107 (1996).

**Acknowledgements.** This work was supported by the Howard Hughes Medical Institute, the NIH and the Dana Foundation.

Correspondence and requests for materials should be addressed to M.F.B. (e-mail:mbear@brown.edu).

## In vivo regulation of axon extension and pathfinding by growth-cone calcium transients

Timothy M. Gomez & Nicholas C. Spitzer

Department of Biology and Center for Molecular Genetics, University of California at San Diego, La Jolla, California 92093-0357, USA

Growth cones at the tips of extending neurites migrate through complex environments in the developing nervous system and guide axons to appropriate target regions using local cues<sup>1,2</sup>. The intracellular calcium concentration ([Ca<sup>2+</sup>]<sub>i</sub>) of growth cones correlates with motility *in vitro*<sup>3–7</sup>, but the physiological links

between environmental cues and axon growth *in vivo* are unknown. Here we report that growth cones generate transient elevations of  $[Ca^{2+}]_i$  as they migrate within the embryonic spinal cord and that the rate of axon outgrowth is inversely proportional to the frequency of transients. Suppressing  $Ca^{2+}$  transients by photorelease of a  $Ca^{2+}$  chelator accelerates axon extension, whereas mimicking transients with photorelease of  $Ca^{2+}$  slows otherwise rapid axonal growth. The frequency of  $Ca^{2+}$  transients is cell-type specific and depends on the position of growth cones along their pathway. Furthermore, growth-cone stalling and axon retraction, which are two important aspects of pathfinding<sup>8–10</sup>, are associated with high frequencies of  $Ca^{2+}$  transients. Our results indicate that environmentally regulated growth-cone  $Ca^{2+}$  transients control axon growth in the developing spinal cord.

We examined the development of axonal projections and rate of axon elongation by dorsal Rohon–Beard neurons, ventral motor neurons, as well as dorsolateral ascending interneurons (DLAs) and ascending interneurons, identifying each by cell-body position and axon projection pattern (Fig. 1a, b)<sup>11</sup>. The dorsal longitudinal axon fascicle (DLF) appears first and forms in 2 h by simultaneous initiation of Rohon–Beard axons along the length of the spinal cord. Ventral motor neurons appear within 1 h of the earliest Rohon–Beard axons and form the ventral longitudinal fascicle (VLF) gradually from anterior to posterior over a period of more than 8 h. Comparison of axon lengths of several neuronal classes at successive embryonic stages suggests that DLAs, which do not fasciculate, grow more slowly than Rohon–Beard axons and ventral motor neurons (Fig. 1c–f). To determine whether axons grow at different rates as they navigate

and to assess the relationship between axon growth and  $Ca^{2+}$  dynamics, we examined Fluo-3-loaded growth cones in the spinal cord with time-lapse confocal microscopy.

The rate of axon outgrowth is inversely related to the frequency of endogenous growth-cone  $Ca^{2+}$  transients. Growth cones producing a high frequency of  $Ca^{2+}$  transients migrate slowly or retract (Fig. 2a, b, e), whereas growth cones generating a low frequency of  $Ca^{2+}$  transients migrate rapidly (Fig. 2c, d, e). Moreover, growth cones of individual classes of neuron that change their transient frequency correspondingly accelerate or decelerate (Fig. 2a, b, e).

To determine whether  $Ca^{2+}$  transients are necessary for proper axon extension in the spinal cord, we suppressed elevations of  $[Ca^{2+}]_i$  in identified growth cones by uncaging the photoactivatable  $Ca^{2+}$  chelator diazo-2 (caged-BAPTA) throughout entire neurons to prevent dilution by diffusion. Photoactivation of diazo-2 in DLA growth cones exhibiting high frequencies of  $Ca^{2+}$  transients leads to immediate and prolonged suppression of  $Ca^{2+}$  transients, which lasts up to 45 min, and an increased rate of outgrowth (Fig. 3a–e;  $n = 5$ ). In contrast, photoactivation of diazo-2 in rapidly elongating axons of ascending interneurons that extend along the VLF causes no significant change in growth rate, direction or  $Ca^{2+}$  dynamics (Fig. 3e;  $n = 5$ ). Localized release of BAPTA in the spinal cord was detected using anti-BAPTA antibodies<sup>12</sup> (Fig. 3b inset; a gift of O. Jones). In similar experiments, application of membrane-permeant BAPTA AM (100 nM) to fluorescein isothiocyanate (FITC)–dextran-labelled spinal neurons causes acceleration of axon growth from DLAs without affecting outgrowth of Rohon–Beard or ascending-interneuron axons (Fig. 3f, g;  $n = 5$ ).

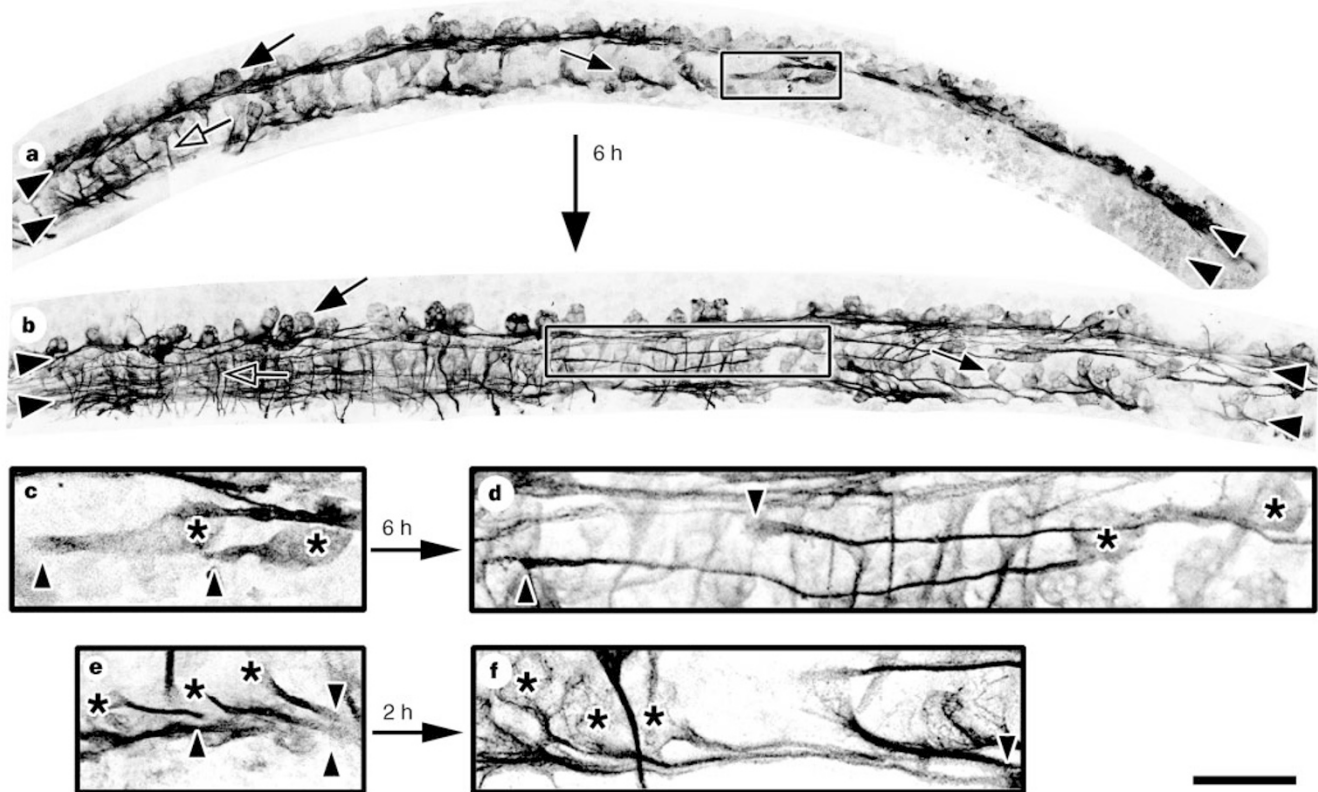


**Figure 1** Rapid assembly and simple structure of the embryonic *Xenopus* spinal cord visualized in confocal Z-series reconstructions of immunofluorescently labelled  $\beta$ -tubulin in whole mounts. **a, b**, Early outgrowth of axons and fascicle formation. **a**, Stage 21. Rohon–Beard axons (large arrow) form the DLF (upper arrowhead), whereas ascending-interneuron (not seen) and ventral motor neuron (small arrow) axons comprise the partially assembled VLF (lower arrowhead). DLA axons ascend between the two primary fascicles (box) and commissural interneurons (open arrow) project midline-crossing axons perpendicular to the

long axis of the spinal cord. **b**, Stage 26. The same classes of neuron are identified. **c–f**, High-magnification views of equivalently anterior–posterior regions of spinal cords used to estimate axonal growth rates for DLAs and ventral motor neurons. Asterisks and arrowheads mark cell bodies and growth cones, respectively. **c, d**, Boxes from **a, b** show that DLA axons grow an average of 138  $\mu\text{m}$  in 6 h (23  $\mu\text{m h}^{-1}$ ). **e, f**, Ventral motor neurons (low magnification views not shown) grow 100  $\mu\text{m}$  in just 2 h (50  $\mu\text{m h}^{-1}$ ). Scale bar represents 100  $\mu\text{m}$  (**a, b**) and 33  $\mu\text{m}$  (**c–f**);  $n = 6$ .



To test whether  $\text{Ca}^{2+}$  transients are sufficient to slow the rate of axon growth, we used NP-EGTA (caged- $\text{Ca}^{2+}$ ) to impose  $\text{Ca}^{2+}$  elevations at defined frequencies in rapidly migrating growth cones not generating  $\text{Ca}^{2+}$  transients. Restricting the ultraviolet flash to growth cones allowed us to produce up to ten brief, localized  $\text{Ca}^{2+}$  elevations, probably as a result of replenishment of unphotolysed NP-EGTA by diffusion from the axons. Imposing  $\text{Ca}^{2+}$  transients in rapidly migrating growth cones of Rohon–Beard neurons, ventral motor neurons and ascending interneurons leads to a decrease in growth rate, which recovers within 5 min after transients are terminated (Fig. 3h–k;  $n = 15$ ). Consistent with observations of endogenous  $\text{Ca}^{2+}$  transients, the rate of axon growth is inversely dependent on the frequency of  $\text{Ca}^{2+}$  transients over the natural range (Fig. 3l).

Because axon extension often stalls or growth cones retract at ‘decision regions’ *in vivo*<sup>8–10,13,14</sup>, we determined whether these rate changes involve increased frequencies of  $\text{Ca}^{2+}$  transients. When growth cones of ventral motor neurons and ascending interneurons make sharp turns to join the VLF, they stall for up to 1 h as they approach (mean  $\pm$  standard error: angle of approach,  $72 \pm 6^\circ$ ; rate of elongation,  $5 \pm 9 \mu\text{m h}^{-1}$ ;  $n = 5$ ), after which they turn onto the fascicle and maintain a high rate of elongation (Fig. 4a–d;  $37 \pm 11 \mu\text{m h}^{-1}$ ;  $n = 5$ ). Growth cones exhibit higher frequencies of  $\text{Ca}^{2+}$  transients during stalled growth (Fig. 4e–h;  $60 \pm 6^\circ$ ;  $10 \pm 1$  transients  $\text{h}^{-1}$ ;  $15 \pm 4 \mu\text{m h}^{-1}$ ;  $n = 6$ ), which subside after they

turn and accelerate onto the VLF (0 transients  $\text{h}^{-1}$ ;  $52 \pm 4 \mu\text{m h}^{-1}$ ;  $n = 11$ ). When axons approach the VLF/floorplate margin at a shallow angle, growth cones do not generate  $\text{Ca}^{2+}$  transients or slow as they turn onto the VLF ( $36 \pm 1^\circ$ ; 0 transients  $\text{h}^{-1}$ ;  $57 \pm 5 \mu\text{m h}^{-1}$ ;  $n = 3$ ), suggesting that a critical angle of approach is necessary for transients to be triggered. These results confirm that spontaneous transients are not necessary for growth-cone turning through shallow angles<sup>15</sup>, but indicates that they appear to prevent inappropriate extension of axons into the floorplate. Stalling at larger approach angles may be due to more extensive sampling of repellent cues in the floorplate and less extensive sampling of attractant cues along the VLF.

Several lines of evidence suggest that the frequency of  $\text{Ca}^{2+}$  transients in growth cones is determined by their immediate environment. All four classes of growth cone possess comparable  $\text{Ca}^{2+}$ -buffering and downstream-effector mechanisms, as reprogramming  $\text{Ca}^{2+}$  dynamics with caged  $\text{Ca}^{2+}$  or BAPTA produces similar behavioural responses in Rohon–Beard neurons, ventral motor neurons, ascending interneurons and DLAs.  $\text{Ca}^{2+}$ -transient frequencies are specific for each class of neuron and depend on the position of growth cones in the developing spinal cord. Growth cones of Rohon–Beard neurons, ventral motor neurons and ascending interneurons on fascicles show a low incidence and frequency of transients and migrate rapidly (Fig. 2e; 3/23;  $0.4 \pm 0.2$  transients  $\text{h}^{-1}$ ;  $52 \pm 3 \mu\text{m h}^{-1}$ ). In contrast, growth cones of DLAs ascending

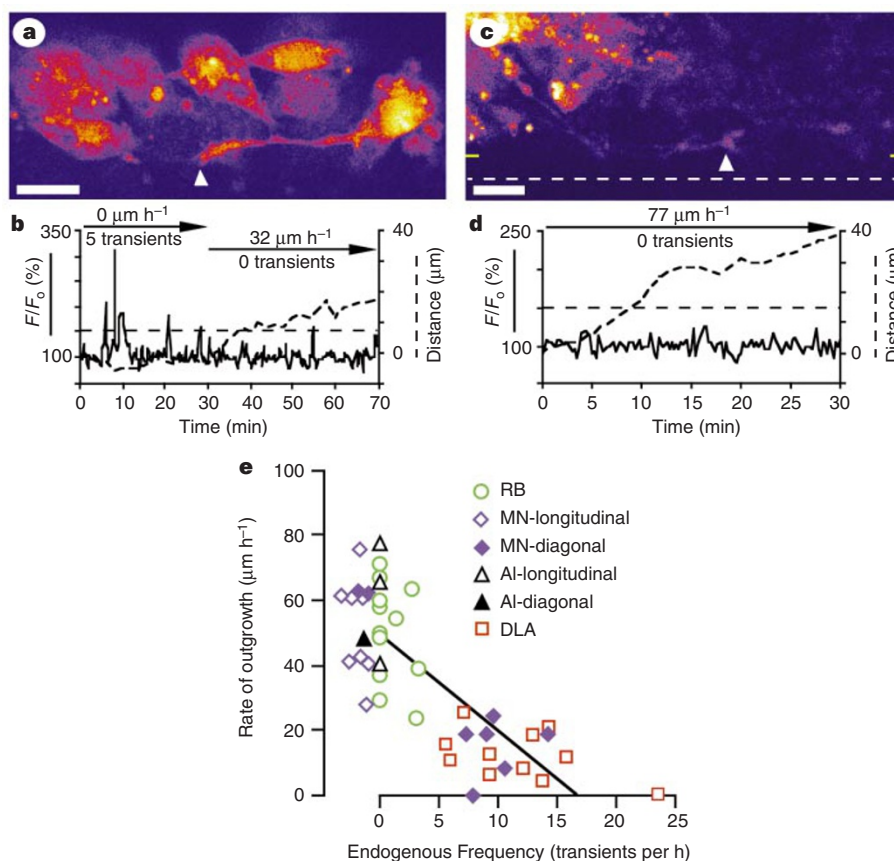


**Figure 2** The rate of axon extension is inversely proportional to the frequency of spontaneous  $\text{Ca}^{2+}$  transients. **a**, DLA growth cone (arrowhead) ascending near the sulcus limitans; stage 22. **b**, Fluo-3 fluorescence and rate of outgrowth of the DLA growth cone in **a** show that it is immobile during the first 30 min of imaging when five  $\text{Ca}^{2+}$  transients exceeding 150% of baseline are produced (including a single spike; dashed line indicates threshold), but extends after transients subside. Changes in fluorescence ( $F$ ) are expressed relative to baseline ( $F_0$ ). **c**, Ventral motor-neuron growth cone (arrowhead) descending along the VLF (yellow bars at margins; dashed white line indicates spinal cord/notochord

boundary); stage 23. **d**, The growth-cone fluorescence in **c** never exceeds threshold, indicating an absence of  $\text{Ca}^{2+}$  transients, and the rate of axon extension is rapid. Scale bar in **a**, **c** represents  $20 \mu\text{m}$ . **e**, Rate of outgrowth is inversely related to transient frequency, which depends on cell type and growth-cone position. RB, Rohon–Beard neurons; MN, ventral motor neurons; AI, ascending interneurons;  $n = 43$  neurons at stages 21–25. Points at 0 transients  $\text{h}^{-1}$  are offset to avoid superposition. Slope of fitted line =  $-3.0$ , correlation coefficient ( $r$ ) =  $0.78$ ,  $P < 0.0001$ .

between the two primary fascicles display a high incidence and frequency of  $\text{Ca}^{2+}$  transients and migrate slowly ( $11/11$ ;  $12 \pm 2$  transients  $\text{h}^{-1}$ ;  $12 \pm 2 \mu\text{m h}^{-1}$ ). Additionally, growth cones of ventral motor neurons show a high incidence and frequency of  $\text{Ca}^{2+}$  transients and stall before joining the VLF ( $6/8$ ;  $10 \pm 1$  transients  $\text{h}^{-1}$ ;

$15 \pm 4 \mu\text{m h}^{-1}$  as noted above), but show no transients once on the fascicle where they exhibit a rapid rate of growth ( $8/8$ ; 0 transients  $\text{h}^{-1}$ ;  $50 \pm 6 \mu\text{m h}^{-1}$ ). Growth-cone  $\text{Ca}^{2+}$  transients may be suppressed by molecules such as laminin and L1 that are expressed on axons<sup>16,17</sup>, and stimulated by molecules such as netrin that are expressed in the

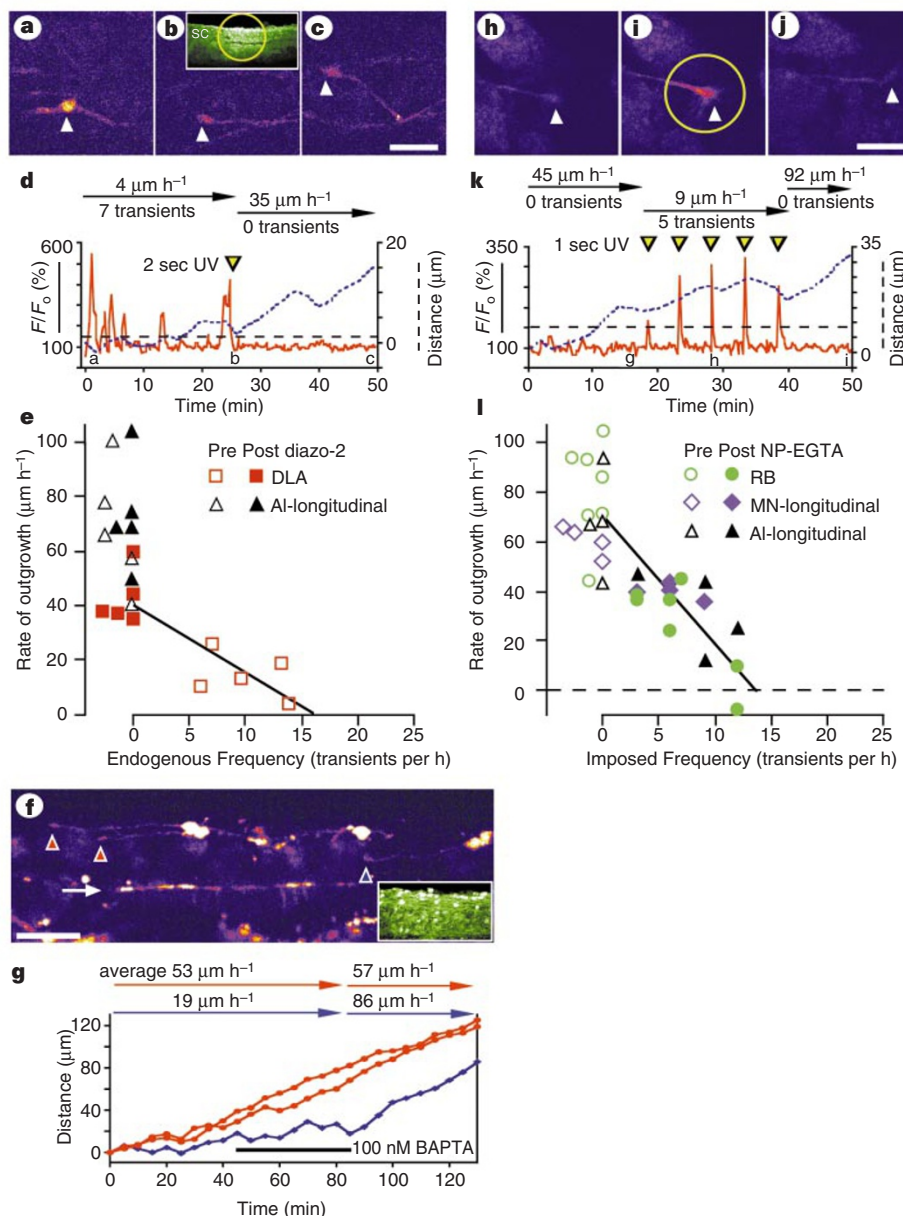


**Figure 3** Suppression or imposition of  $\text{Ca}^{2+}$  transients with photoactivatable compounds alters rates of axon extension. **a–d**, Blocking  $\text{Ca}^{2+}$  transients by photoactivation of caged-BAPTA accelerates axon outgrowth from a DLA. Growth cone (arrowheads) co-loaded with Fluo-3 AM and diazo-2 AM; images at times indicated in **d**. Inset in **b** shows local uncaging of BAPTA in the spinal cord (sc) revealed with anti-BAPTA antibodies. Yellow circle marks the size and position of the ultraviolet spot. Stage 24; scale bar represents  $20 \mu\text{m}$  ( $300 \mu\text{m}$  for inset). **d**, This growth cone initially generates  $\text{Ca}^{2+}$  transients and migrates slowly. After photoactivation of diazo-2 (yellow arrowhead), transients are abolished and the axon elongates rapidly. **e**, Rate of axon outgrowth is inversely related to transient frequency and increases selectively in DLAs but not in ascending interneurons (AIs) when endogenous transients are quenched.  $n = 10$  neurons at stages 22–25. Slope of fitted line for DLAs only =  $-2.5$ ,  $r = 0.70$ ,  $P < 0.005$ . **f**, Conventional BAPTA similarly speeds axonal growth in DLAs, but has no effect on Rohon-Beard axons. Two Rohon-Beard axon growth cones (red arrowheads) and one DLA growth cone (blue arrowhead) in a FITC-dextran-labelled spinal cord. Ubiquitous loading of BAPTA was confirmed using anti-BAPTA antibodies (inset). Arrow

indicates spinal cord/notochord boundary. Stage 25; scale bar represents  $100 \mu\text{m}$  ( $170 \mu\text{m}$  for inset). **g**, Rate of outgrowth of axons in **f**. A slowly migrating DLA growth cone accelerates after loading with BAPTA, but two rapidly migrating Rohon-Beard growth cones are unaffected (combined data for diazo-2 and BAPTA experiments:  $n = 8$  DLAs,  $14 \pm 3 \mu\text{m h}^{-1}$  pre-chelation and  $61 \pm 9 \mu\text{m h}^{-1}$  post-chelation,  $P < 0.001$ ;  $n = 8$  ascending-interneuron and Rohon-Beard axons,  $59 \pm 8 \mu\text{m h}^{-1}$  pre-chelation and  $65 \pm 9 \mu\text{m h}^{-1}$  post-chelation,  $P = 0.08$ ). **h–j**, Imposing  $\text{Ca}^{2+}$  transients on growth cones of Rohon-Beard neurons, ventral motor neurons and ascending interneurons with caged- $\text{Ca}^{2+}$  reduces axon growth rate. **h–j**, Rohon-Beard growth cone (arrowheads) co-loaded with Fluo-3 AM and NP-EGTA AM; images at times indicated in **k**. Yellow circle indicates the ultraviolet spot. Stage 23; scale bar represents  $20 \mu\text{m}$ . **k**, Fluorescence changes and distance migrated for growth cone in **h–j**. Axon extension slows when ultraviolet flashes are delivered at 5-min intervals (yellow arrowheads). **l**, Rate of axon outgrowth is inversely related to imposed transient frequency. RB, Rohon-Beard neurons; MN, ventral motor neurons; AI, ascending interneurons;  $n = 15$  neurons at stages 22–25. Slope of fitted line =  $-5.1$ ,  $r = 0.76$ ,  $P < 0.0001$ .



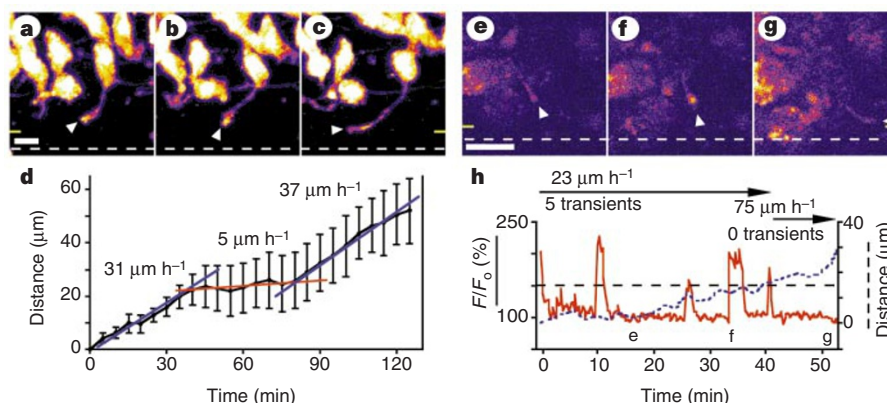


**Figure 4** Growth cones directly approaching the VLF generate increased frequencies of  $\text{Ca}^{2+}$  transients and stall before turning onto this fascicle. **a–c**, An FITC-dextran-labelled growth cone of an ascending interneuron before, during and after stalling at the VLF (arrowheads indicate the position and angle of approach; other markings as in Fig. 2). Shortly after axon initiation, the growth cone begins turning anteriorly (**a**); its orientation varies during stalled growth (**b**), and it finally accelerates as it turns onto the VLF and maintains a high rate of growth (**c**). Stage 23; scale bar represents  $20 \mu\text{m}$ . **d**, Velocities of growth cones of

five ventral motor neurons and ascending interneurons at stages 22–24 time-locked to the start of each stall period. **e–g**, Ventral motor neuron growth cone (arrowheads) loaded with Fluo-3 AM; images at times indicated in **h**. The growth cone advances slowly and exhibits  $\text{Ca}^{2+}$  transients as it directly approaches the VLF (**e, f**), then accelerates as it orientates longitudinally to descend on the VLF (**g**). Stage 25; scale bar represents  $20 \mu\text{m}$ . **h**, Fluorescence changes and distance migrated for growth cone in **e–g**.

floorplate<sup>18,19</sup>. Consistent with this view, growth cones show a low incidence and frequency of transients and extend long neurites when neurons are cultured on laminin (52%;  $\sim 2$  transients  $\text{h}^{-1}$ ;  $219 \pm 12 \mu\text{m}$ ;  $n > 100$ ; T.M.G. and N.C.S., unpublished data), but a high incidence and frequency and short neurites on tissue-culture plastic (100%,  $\sim 8$  transients  $\text{h}^{-1}$ ,  $81 \pm 3 \mu\text{m}$ ;  $n > 100$ ; ref. 7). Furthermore, endogenous growth-repulsive molecules, such as chondroitin sulphate proteoglycans, stimulate  $\text{Ca}^{2+}$  transients in growth cones of dorsal-root-ganglion neurons<sup>20</sup>. Thus, transient elevations of intracellular  $\text{Ca}^{2+}$  in growth cones are a natural signalling mechanism that regulates both the rate of axon extension and guidance of axons in the developing spinal cord. Control of both migration<sup>21</sup> and axon outgrowth by transient elevations of  $[\text{Ca}^{2+}]_i$  allows neurons to respond in a cell-specific and graded fashion to the dynamic environment of molecular gradients, guideposts and boundaries in the nervous system. □

## Methods

**Embryo preparation and loading.** Local regions of spinal cord were loaded selectively with Fluo-3 AM (Bio-Rad), to permit visualization of labelled growth cones extending into unlabelled regions of the cord. Stage 21–25/26 embryos<sup>22</sup> were dissected in a modified Ringer's solution<sup>23</sup> at  $20^\circ\text{C}$ . Anterior or posterior portions of skin and somites were removed from one side of the spinal cord with a sharpened tungsten needle and collagenase B ( $0.1 \text{ mg ml}^{-1}$ ). Partially exposed spinal cords were then bathed in  $10 \mu\text{M}$  Fluo-3 AM (with  $0.04\%$  pluronic acid/ $0.4\%$  dimethyl sulphoxide (DMSO) in modified Ringer's solution) for 1 h at  $20^\circ\text{C}$ . After washing in modified Ringer, the remaining skin and somites were removed, revealing unlabelled portions of the cord in which labelled growth cones could be visualized, and embryos were pinned down laterally on a Sylgard dish and perfused with modified Ringer at  $1 \text{ ml min}^{-1}$ . Loading of spinal neurons with diazo-2 AM ( $100 \text{ nM}$ , Molecular Probes) or NP-EGTA AM ( $5 \mu\text{M}$ , Molecular Probes) in conjunction with Fluo-3 was done in the same manner. For other experiments, neurons were labelled by injection of individual blastomeres at the 32-cell stage with FITC-dextran (relative molecular mass 10,000, Molecular Probes).

**Image acquisition and analysis.** Fluorescent images of labelled growth cones, axons and cell bodies were captured at 15-s intervals using a Bio-Rad MRC 600 argon laser confocal system and  $\times 40$  Neofluor water immersion lens. To minimize photodynamic damage, the laser was operated under low power and light was attenuated to no greater than 1% using neutral density filters. Baseline growth-cone  $[\text{Ca}^{2+}]_i$  and rate of axon outgrowth were monitored for at least 15 min before release of caged compounds with 1–2-s flashes of ultraviolet light

(340–380 nm) at different frequencies. Image sequences were analysed with NIH Image software (W. Rasband, NIH). Rate of outgrowth was determined at 2–5-min intervals by measuring axon length from the cell body to the leading margin of the growth cone, or by determining the movement of the leading edge of the growth cone relative to several stationary landmarks using a coordinate-based macro (I. Hsieh, UCSD). To assess changes in  $[\text{Ca}^{2+}]_i$ , the average pixel intensity within user-defined regions of at least 100 pixels within growth cones was quantified at 15-s intervals, background subtracted and normalized to baseline. Fluorescence increases to  $>150\%$  of baseline were recognized as  $\text{Ca}^{2+}$  transients, and were readily distinguished from noise (mean  $<130\%$  of baseline). In most cases,  $\text{Ca}^{2+}$  transients were waves (refs 7, 8) recognized by their localization to the growth cone, their kinetics ( $\sim 30 \text{ s}$  to peak), and their return to baseline; these characteristics also distinguished them from morphological movements. Images are pseudocoloured with peak elevations of  $[\text{Ca}^{2+}]_i$  indicated in white/gold.

**Whole-mount  $\beta$ -tubulin and BAPTA immunocytochemistry and imaging.** Tubulin immunocytochemistry was done as described<sup>24</sup>. The spinal cord was visualized by projecting a confocal Z-series image stack (20–30 slices,  $3 \mu\text{m}$  depth). For BAPTA and diazo-2 immunocytochemistry, embryos were incubated in EDC fixative (Pierce;  $20 \text{ mg ml}^{-1}$  in phosphate-buffered saline (PBS)) overnight at  $4^\circ\text{C}$ , washed in PBS–glycine, and reacted with primary antibody ( $1:500$  rabbit anti-BAPTA<sup>25</sup>; O. Jones, University of Toronto) and secondary antibody (FITC–goat anti-rabbit, Jackson).

Received 26 October; accepted 30 November 1998.

- Goodman, C. S. & Shatz, C. Developmental mechanisms that generate precise patterns of neuronal connectivity. *Cell/Neuron* **72/10**, 77–98 (1993).
- Tessier-Lavigne, M. & Goodman, C. S. The molecular biology of axon guidance. *Science* **274**, 1123–1133 (1996).
- Gomez, T. M., Snow, D. M. & Letourneau, P. C. Characterization of spontaneous calcium transients in nerve growth cones and their effect on growth cone migration. *Neuron* **14**, 1233–1246 (1995).
- Kater, S. B. & Mills, L. R. Regulation of growth cone behavior by calcium. *J. Neurosci.* **11**, 891–899 (1991).
- Kater, S. B., Mattson, M. P., Cohan, C. & Connor, J. Calcium regulation of the neuronal growth cone. *Trends Neurosci.* **11**, 315–321 (1988).
- Gu, X., Olson, E. C. & Spitzer, N. C. Spontaneous neuronal calcium spikes and waves during early differentiation. *J. Neurosci.* **14**, 6325–6335 (1994).
- Gu, X. & Spitzer, N. C. Distinct aspects of neuronal differentiation encoded by frequency of spontaneous  $\text{Ca}^{2+}$  transients. *Nature* **375**, 784–787 (1995).
- Godement, P., Wang, L. C. & Mason, C. A. Retinal axon divergence in the optic chiasm: dynamics of growth cone behavior at the midline. *J. Neurosci.* **14**, 7024–7039 (1994).
- Ghosh, A. & Shatz, C. J. Pathfinding and target selection by developing geniculocortical axons. *J. Neurosci.* **12**, 39–55 (1992).
- Myers, P. Z. & Bastiani, M. J. Growth cone dynamics during the migration of an identified commissural growth cone. *J. Neurosci.* **13**, 127–143 (1993).
- Roberts, A. & Clarke, J. D. W. The neuroanatomy of an amphibian embryo spinal cord. *Phil. Trans. R. Soc. Lond. B* **296**, 195–212 (1982).
- Tymianski, M., Sattler, R., Bernstein, G. & Jones, O. T. Preparation, characterization and utility of a novel antibody for resolving the spatial and temporal dynamics of the calcium chelator BAPTA. *Cell Calcium* **22**, 111–120 (1997).

13. Bovolenta, P. & Mason, C. A. Growth cone morphology varies with position in the developing mouse visual pathway from retina to first targets. *J. Neurosci.* **7**, 1447–1460 (1987).
14. Tosney, K. W. & Landmesser, L. T. Development of the major pathways for neurite outgrowth in the chick hindlimb. *Dev. Biol.* **109**, 193–214 (1985).
15. Zheng, J. Q., Felder, M., Connor, J. A. & Poo, M. Turning of nerve growth cones induced by neurotransmitters. *Nature* **368**, 140–144 (1994).
16. Lagenaur, C. & Lemmon, V. An L1-like molecule, the 8D9 antigen, is a potent substrate for neurite extension. *Proc. Natl Acad. Sci. USA* **84**, 7753–7757 (1987).
17. Hagg, T., Portera-Cailliau, C., Jucker, M. & Engvall, E. Laminins of the adult mammalian CNS; laminin- $\alpha$ 2 (merosin M-) chain immunoreactivity is associated with neuronal processes. *Brain Res.* **764**, 17–27 (1997).
18. Varela-Echavarría, A., Tucker, A., Puschel, A. W. & Guthrie, S. Motor axon subpopulations respond differentially to the chemorepellents netrin-1 and semaphorin D. *Neuron* **18**, 193–207 (1997).
19. Colamarino, S. A. & Tessier-Lavigne, M. The axonal chemoattractant netrin-1 is also a chemorepellent for trochlear motor axons. *Cell* **81**, 621–629 (1995).
20. Snow, D. M., Atkinson, P., Hassinger, T., Kater, S. B. & Letourneau, P. C. Growth cone intracellular calcium levels are elevated upon contact with sulfated proteoglycans. *Dev. Biol.* **166**, 87–100 (1994).
21. Komuro, H. & Rakic, P. Intracellular  $\text{Ca}^{2+}$  fluctuations modulate the rate of neuronal migration. *Neuron* **17**, 275–285 (1996).
22. Nieuwkoop, J. M. & Faber, J. *Normal Table of Xenopus Laevis (Daudin): A Systematic and Chronological Survey of the Development of the Fertilized Egg Till the End of Metamorphosis* 2nd edn (North-Holland, Amsterdam, 1967).
23. Chien, C. B., Rosenthal, D. E., Harris, W. A. & Holt, C. E. Navigational errors made by growth cones without filopodia in the embryonic *Xenopus* brain. *Neuron* **11**, 237–251 (1993).
24. McFarlane, S., McNeill, L. & Holt, C. E. FGF signaling and target recognition in the developing *Xenopus* visual system. *Neuron* **15**, 1017–1028 (1995).
25. Tymianski, M. *et al.* A novel use for a carbodiimide compound for the fixation of fluorescent and non-fluorescent calcium indicators *in situ* physiological experiments. *Cell Calcium* **21**, 175–183 (1997).

**Acknowledgements.** We thank S. Watt and I. Hsieh for technical assistance, and M. Ferrari and M.-M. Poo for comments on the manuscript. Research supported by a NIH NINDS fellowship to T.M.G. and grant to N.C.S.

Correspondence and requests for materials should be addressed to T.M.G. (email: tgomez@biomail.ucsd.edu). Quicktime movies of  $\text{Ca}^{2+}$  imaging *in vivo* can be viewed at <http://www-biology.ucsd.edu/~tgomez/>.

## Secondary V(D)J recombination in B-1 cells

Xiao-Feng Qin<sup>\*</sup>, Stephan Schwerts<sup>†</sup>, Wong Yu<sup>\*</sup>, Fotini Papavasiliou<sup>\*</sup>, Heikyung Suh<sup>\*‡</sup>, Andre Nussenzweig<sup>§</sup>, Klaus Rajewsky<sup>†</sup> & Michel C. Nussenzweig<sup>\*‡</sup>

<sup>\*</sup> Laboratory of Molecular Immunology, and <sup>‡</sup> Howard Hughes Medical Institute, The Rockefeller University, New York, New York 10021, USA

<sup>§</sup> Experimental Immunology Branch, National Cancer Institute, National Institutes of Health, Bethesda, Maryland 20892, USA

<sup>†</sup> Institute for Genetics, University of Cologne, Weyertal 50931, Germany

B-1 B cells are a self-renewing population of B cells that differ from conventional B cells (B-2 cells) in that they are particularly predisposed to auto-antibody production<sup>1–3</sup>. Although much is known about the signalling pathways that control B-1-cell growth and development (reviewed in ref. 4), less is known about why these cells are prone to produce autoreactive antibodies. Here we show that B-1 cells, like germinal-centre B cells<sup>5–8</sup>, can express recombinase-activating genes 1 and 2 (*RAG1* and *RAG2*) and undergo secondary V(D)J recombination of immunoglobulin genes. In addition, B cells from autoimmune-prone NZB mice show high levels of RAG messenger RNA and recombination. We propose that secondary immunoglobulin-gene rearrangements outside organized lymphoid organs may contribute to the development of autoreactive antibodies.

To study recombination of immunoglobulin genes in B-1 cells, we analysed mice that carry replacements of immunoglobulin heavy- and light-chain variable genes (B1-8H1<sup>+/–</sup> and 3-83 $\kappa$ 1<sup>+/–</sup> heterozygotes)<sup>9,10</sup>. The replacement genes, VHB1-8 and VK3-83, excluded the recombination and expression of endogenous variable genes on the wild-type allele during early B-cell development, and most bone-marrow and spleen B cells in these heterozygotes expressed the Ac146 idiotype, which is encoded by the VHB1-8 and VK3-83 gene combination<sup>9,10</sup>. When these mice were 4 months old, less than 5% of the B cells in the spleen had the phenotype IgM<sup>+</sup>Ac146<sup>–</sup> (Fig. 1a and refs 10, 11). In contrast, many IgM<sup>+</sup> peritoneal B cells were idiotype-negative (Fig. 1a). The number of IgM<sup>+</sup>Ac146<sup>–</sup> B cells

in the peritoneal cavity of B1-8H1<sup>+/–</sup>3-83 $\kappa$ 1<sup>+/–</sup> mice varied and tended to increase with age, ranging from 8% in 3-week-old mice to 45% in 4–6-month-old mice (Fig. 1a and data not shown). Spontaneous co-expression of endogenous and transgenic antigen receptors in peritoneal B cells was first seen in mice expressing transgenic immunoglobulin<sup>12</sup> and loss of idiotype expression on peritoneal B cells has been reported in two other independently derived strains carrying replacements of immunoglobulin genes<sup>13,14</sup>.

Does a specific population of B cells in the peritoneum lose idiotype expression? To determine this, we stained peritoneal cells with a combination of anti-IgM, anti-B220 and anti-idiotype

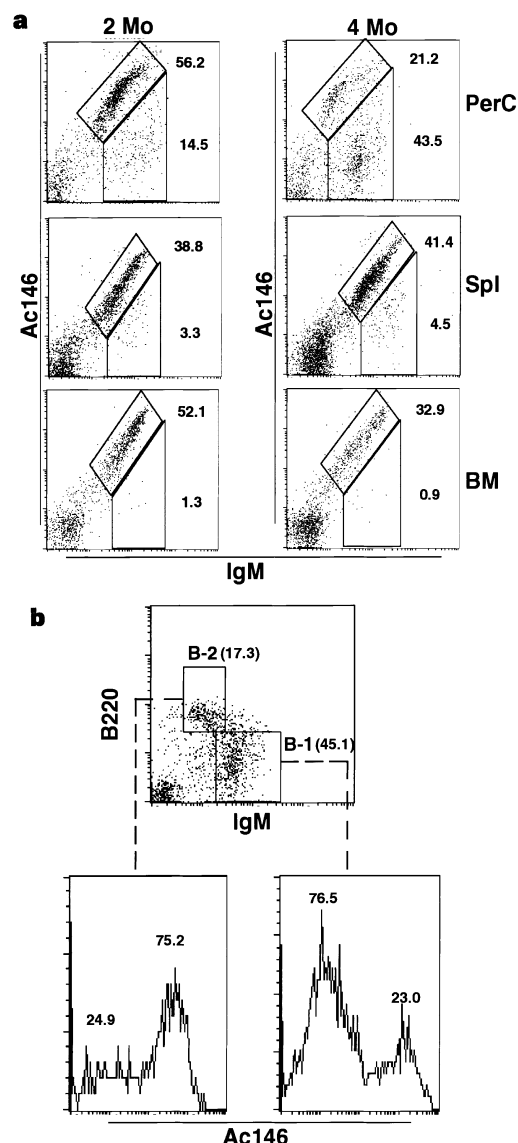


**Figure 1** Loss of expression of the Ac146 idiotype on peritoneal B cells. **a**, Cells prepared from the peritoneal cavity (PerC), spleen (Spl) and bone marrow (BM) of 2-month-old (2 Mo) and 4-month-old (4 Mo) B1-8H1<sup>+/–</sup>3-83 $\kappa$ 1<sup>+/–</sup> mice were stained with anti-IgM and anti-Ac146 antibodies and analysed by flow cytometry. The numbers indicate the percentages of IgM<sup>+</sup>Ac146<sup>+</sup> and IgM<sup>+</sup>Ac146<sup>–</sup> cells (outlined) in the live-lymphocyte gate. **b**, Peritoneal cells from 4-month-old B1-8H1<sup>+/–</sup>3-83 $\kappa$ 1<sup>+/–</sup> mice were stained with anti-IgM, anti-B220 and anti-Ac146 antibodies and analysed by flow cytometry. IgM<sup>high</sup>B220<sup>low</sup> B-1 cells and IgM<sup>low</sup>B220<sup>high</sup> B-2 cells were gated as indicated. The numbers in parentheses are the percentages of B-1 and B-2 cells. Expression of the Ac146 idiotype on the gated B-1 and B-2 cells is shown in the histograms; the numbers indicate the percentages of Ac146-positive (24.9% and 76.5%, respectively) and -negative (75.2% and 23.0%, respectively) cells in the B-2 and B-1 subpopulations.

polarization of the material by virtue of the polar orientational order imparted to them by the smectic C host<sup>20</sup>. On *trans* → *cis* photoisomerization, however, the *cis* isomers are expelled from the layers, and their contribution to the ferroelectric polarization decreases to near zero, as they are much less strongly orientated by the smectic C medium than *trans* isomers.

In general terms, this work demonstrates nanoscale photocontrol of the positional distribution of a photoactive solute in a smectic medium. The same effect should enable photocontrol of solute diffusion (photochemical pumping) and nanoscale photo-induced concentration of reactive species in smectic materials. Photocontrolled nanophase segregation should have a broad range of potential applications in nanotechnology and in the creation of novel photofunctional materials. Moreover, similar effects may play a role in the photoelectric response of bilayer lipid membranes containing azobenzene chromophores<sup>21</sup>.

We are, at present, unable to identify the specific energetic and/or entropic effects responsible for interlamellar nanophase segregation of *cis*-7AB in 7AB/8CB mixtures. A detailed calculation of distinct contributions to the free energy of a solute molecule (such as 7AB) in a smectic host as a function of position relative to the smectic layers is technically feasible, but would require at least an order of magnitude more computational effort than the present study. Understanding the microscopic mechanisms responsible for the formation of smectic phases is itself an unsolved problem, whose solution faces similar technical challenges, and which similarly falls

into a quite broad class of problems related to the self-assembly of soft condensed matter. Studies such as the present one represent first steps towards addressing these problems in the context of liquid-crystal self-assembly. □

Received 17 July; accepted 14 December 1998.

- De Gennes, P. G. & Prost, J. *The Physics of Liquid Crystals* (Clarendon, Oxford, 1993).
- Rieker, T. P. Organic lyotropic lamellar liquid crystals. *Liq. Cryst.* **19**, 497–500 (1995).
- Guymon, C. A. *et al.* Effects of monomer structure on their organization and polymerization in a smectic liquid crystal. *Science* **275**, 57–59 (1997).
- Folks, W. R. *et al.* Low-power laser induced instabilities in smectic A liquid crystals. *Mol. Cryst. Liq. Cryst.* **261**, 259–270 (1995).
- Folks, W. R., Reznikov, Yu. A., Yarmolenko, S. N. & Lavrentovich, O. D. Light-induced periodic lattice of defects in smectic A and C liquid crystals: structural and dynamical aspects. *Mol. Cryst. Liq. Cryst.* **292**, 183–197 (1997).
- Krentsel, T. A., Lavrentovich, O. D. & Kumar, S. In-situ x-ray measurements of light-controlled layer spacing in a smectic liquid crystal. *Mol. Cryst. Liq. Cryst.* **304**, 463–469 (1997).
- Folks, W. R. *et al.* Photocontrol of smectic spacing. *Mol. Cryst. Liq. Cryst.* **320**, 77–88 (1998).
- Berendsen, H. J. C., Postma, J. P. M., van Gunsteren, W. F., Dinola, A. & Haak, J. R. Molecular dynamics with coupling to an external bath. *J. Chem. Phys.* **81**, 3684–3690 (1984).
- Glaser, M. A., Clark, N. A., Garcia, E. & Walba, D. M. Quantum chemistry based force fields for soft matter. *Spectrochim. Acta A* **53**, 1325–1340 (1997).
- Essman, U. *et al.* A smooth particle mesh Ewald method. *J. Chem. Phys.* **103**, 8577–8593 (1995).
- Allen, M. P. & Tildesley, D. J. *Computer Simulation of Liquids* (Oxford Univ. Press, 1987).
- Tuckerman, M., Berne, B. J. & Martyna, G. J. Reversible multiple time scale molecular dynamics. *J. Chem. Phys.* **97**, 1990–2001 (1992).
- Sexton, J. C. & Weingarten, D. H. Hamiltonian evolution for the hybrid Monte Carlo algorithm. *Nucl. Phys. B* **380**, 665–677 (1992).
- Ikeda, T., Sasaki, T. & Ichimura, K. Photochemical switching of polarization in ferroelectric liquid-crystal films. *Nature* **361**, 428–430 (1993).
- Sasaki, T., Ikeda, T. & Ichimura, K. Photochemical control of properties of ferroelectric liquid crystals: photochemical flip of polarization. *J. Am. Chem. Soc.* **116**, 625–628 (1994).
- Sasaki, T. & Ikeda, T. Photochemical control of properties of ferroelectric liquid crystals. 1. Effect of structure of host ferroelectric liquid crystals on the photochemical switching of polarization. *J. Phys. Chem.* **99**, 13002–13007 (1995).
- Sasaki, T. & Ikeda, T. Photochemical control of properties of ferroelectric liquid crystals. 2. Effect of the structure of guest photoresponsive molecules on the photochemical switching of polarization. *J. Phys. Chem.* **99**, 13008–13012 (1995).
- Sasaki, T. & Ikeda, T. Photochemical control of properties of ferroelectric liquid crystals. 3. Photochemically induced reversible change in spontaneous polarization and electrooptic property. *J. Phys. Chem.* **99**, 13013–13018 (1995).
- Coles, H. J., Walton, H. G., Guillon, D. & Poetti, G. Photomechanically induced phase transitions in ferroelectric liquid crystals. *Liq. Cryst.* **15**, 551–558 (1993).
- Glaser, M. A. *et al.* Computer-aided design of ferroelectric liquid crystals. *Mol. Phys. Rep.* **10**, 26–47 (1995).
- Yamaguchi, H. & Nakanishi, H. Characterization of the preparation process and the photochemical control of electrical properties of bilayer lipid membranes containing azobenzene chromophores. *Biochim. Biophys. Acta* **1148**, 179–184 (1993).

**Acknowledgements.** We thank T. Darden for use of his particle-mesh Ewald code, D. Coleman for help in producing the molecular graphics, and D. Finotello and B. Zalar for discussions. This work was supported by the NSF, the US Air Force Office of Sponsored Research, and the Kent State Liquid Crystal Institute (a grant of computer time).

Correspondence and requests for materials should be addressed to M.A.G. (e-mail: matthew.glaser@colorado.edu).

## The role of mat-forming diatoms in the formation of Mediterranean sapropels

Alan E. S. Kemp\*, Richard B. Pearce\*, Itaru Koizumi†, Jennifer Pike\*‡ & S. Jae Rance\*

\* School of Ocean and Earth Science, University of Southampton, Southampton Oceanography Centre, European Way, Southampton SO14 3ZH, UK

† Division of Earth and Planetary Sciences, Graduate School of Science, Hokkaido University, Sapporo, 060, Japan

The origins of sapropels (sedimentary layers rich in organic carbon) are unclear, yet they may be a key to understanding the influence of climate on ocean eutrophication, the mechanisms of sustaining biological production in stratified waters and the genesis of petroleum source rocks<sup>1–3</sup>. Recent microfossil studies of foraminifera<sup>1</sup> and calcareous nannofossils<sup>2</sup> have focused attention on a deep chlorophyll maximum as a locus for the high

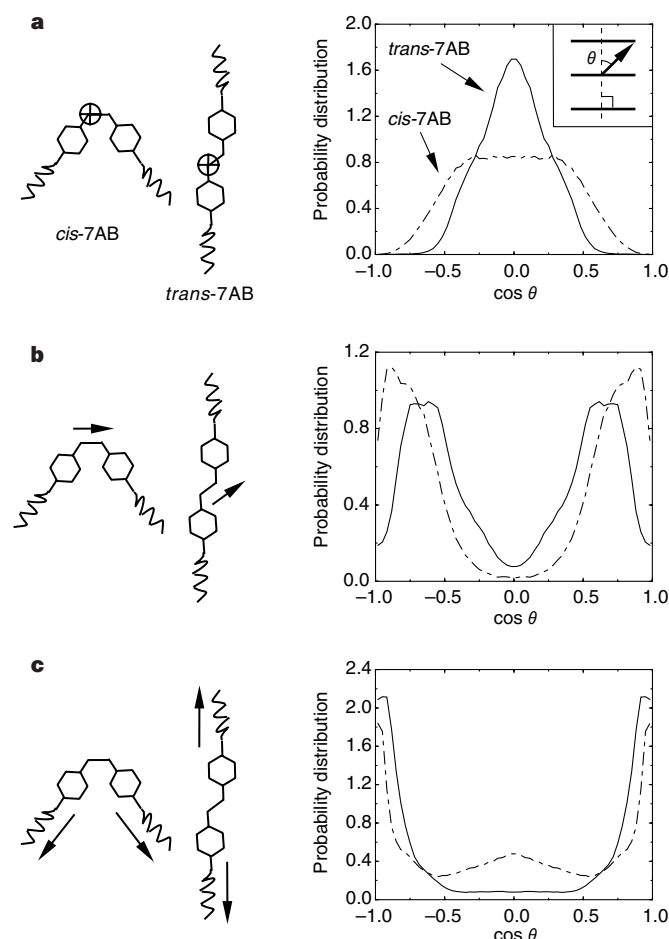


**Figure 4** Orientational distributions for selected portions of the 7AB molecule. Results are shown in terms of the cosine of the angle between a specific intramolecular vector and the layer normal. The distributions for a vector perpendicular to the C-N=N-C plane, for a vector parallel to the N=N bond, and for the end-to-end vectors of the alkyl chains are shown in **a**, **b** and **c**, respectively. Distributions for both *trans*-7AB (solid line) and *cis*-7AB (dot-dashed line) are shown.

‡ Present address: Department of Earth Sciences, University of Wales, Cardiff, PO Box 914, Cardiff CF1 3YE, UK.



production inferred<sup>3</sup> for sapropel formation, but have not identified the agent responsible. Here we report the results of a high-resolution, electron-microscope-based study of a late Quaternary laminated sapropel in which the annual flux cycle has been preserved. We find that much of the production was by diatoms, both mat-forming and other colonial forms, adapted to exploit a deep nutrient supply trapped below surface waters in a stratified water column. Reconstructed organic-carbon and opal fluxes to the sediments are comparable to those at high-productivity sites in today's oceans, and calculations based on diatom Si/C ratios suggest that the high organic-carbon content of sapropels may be entirely accounted for by sedimenting diatoms. We propose that this style of production may have been common in ancient Palaeogene and Cretaceous seas, environments for which conventional appeals to upwelling-driven production to account for the occurrence of diatomites, and some organic-carbon-rich sediments, have never seemed wholly appropriate.

The Mediterranean Sea has provided a focus for the contentious debate over the relative importance of stratification-driven anoxia versus productivity in the origins of organic-carbon-rich sediments. An ingredient that has been largely missing from this debate are inferences from the ecology of diatoms, the world's dominant marine primary producer. This is because the waters of the Mediterranean are highly undersaturated in silica, and the opaline skeletons of siliceous plankton are preserved only rarely in anoxic brine-basins whose waters are buffered and contain higher levels of dissolved silica<sup>4</sup>. Leg 160 of the Ocean Drilling Program (ODP) collected a suite of cores from the eastern Mediterranean that included a critical site (971) in the deepest part of the moat of the Napoli mud volcano on the Mediterranean ridge (Fig. 1). This natural sediment trap has preserved a late Quaternary laminated diatomaceous sapropel (S5) which records the annual flux cycle. We combine a detailed electron-microscope investigation of this sapropel (and diatom micropalaeontology of other sapropels cored during ODP Leg 160) with recent developments in the understanding of the ecology of mat-forming diatoms<sup>5</sup>, and of their significant role in generating massive flux<sup>6,7</sup>, to present a model of the formation of organic-carbon-rich sapropels.

To analyse the composition of individual laminae, we utilized electron-microscope techniques involving back-scattered electron imagery (BSEI) of sediment prepared by fluid-displacive resin-embedding in order to preserve the delicate microfabrics<sup>8</sup>. Having used BSEI to define the laminae (Fig. 2), we then analysed floral assemblages by using topographic electron-microscope imagery of sub-samples taken from counterparts of laminae (Fig. 2) and conventional diatom micropalaeontological preparations sampled, in surgical style, from groups of laminae. The sediment consists of

diatomaceous laminae intercalated with subordinate, variably thick layers of mineralogenic detritus which we interpret to represent either exudates of the Napoli mud volcano or material shed from its flanks in low-density gravity flows. BSEI analysis of a 50-cm section of the sapropel, containing 976 laminae/layers, reveals a regularly recurring couplet of diatomaceous laminae; this couplet consists of a pure, near-monospecific diatom lamina alternating with a lamina composed of a mixed diatom assemblage together with minor coccolith debris (Fig. 2). Most (86%) of the former laminae comprise mat-forming rhizosolenid diatoms with 14% composed of the chain-forming *Hemiaulus hauckii* (Fig. 2) and, occasionally, *Ethmodiscus* sp. Conventional diatom preparations reveal that the rhizosolenids are dominantly *Pseudosolenia calcar-avis* with smaller amounts of *Rhizosolenia styliformis* and rare *R. bergonii* and *R. setigera*<sup>8</sup>. Rhizosolenid diatoms comprise 46% of the total valves counted from 17 samples (see Supplementary Information)<sup>8,9</sup>. The laminae containing mixed diatom assemblages contain mainly *Thalassionema frauenfeldii*, with smaller abundances of *T. nitzschoides*, *Bacteriastrium* spp. and *Chaetoceros* spp. resting spores and few rhizosolenids. Another sample of S5 from ODP Site 967 south of Eratosthenes seamount (Fig. 1) has a similar diatom assemblage (see Supplementary Information) although the frustules have undergone considerable silica dissolution<sup>9</sup>. Similar diatom floras were previously identified in sapropels S4 and S5 from the eastern Mediterranean using conventional micropalaeontological methods<sup>10</sup> (Fig. 1). An early Pleistocene diatomaceous sapropel from ODP Site 969 located near Site 971 on the Mediterranean ridge (Fig. 1) also contains abundant rhizosolenids<sup>9</sup> (see Supplementary Information).

We assume an annual periodicity for the lamina couplets in S5 at Site 971 on the basis of the regular recurrence of the two lamina types, which points to two distinct seasonal episodes of flux. The seasonal flux cycle may be reconstructed by consideration of the ecology of the diatoms involved. The most common diatom within the mixed assemblage laminae, *T. frauenfeldii*, has been recorded as the dominant diatom in the winter/early-spring period in the modern eastern Mediterranean<sup>11,12</sup>, and *T. nitzschoides*, *Bacteriastrium* spp. and *Chaetoceros* spp. resting spores are also common<sup>12</sup>. The intact nature of many of the diatoms in these laminae suggests the rapid flocculation and sinking associated with blooms; such processes are well known, both from water-column observation<sup>13</sup> and experimental mesocosm study, and from BSEI studies of sedimentary laminae<sup>14</sup>. We may suppose, therefore, that the mixed-assemblage lamina represents the fallout from production that occurred during the winter-spring period.

The interpretation of the rhizosolenid laminae is not so straightforward. In fact, both *P. calcar-avis* and *H. hauckii* are characteristic of the modern Mediterranean, but typically occur in low abundances through nutrient-poor conditions during the months of summer stratification (May–October)<sup>12,15</sup>. Indeed, large rhizosolenid diatoms and *Hemiaulus* spp. have been generally regarded as slow-growing and characteristic of the sparse flora of oligotrophic waters<sup>15</sup>. Laboratory and field studies have demonstrated that both rhizosolenids and *Hemiaulus* spp. have specific adaptations for stratified oligotrophic waters including symbiosis with nitrogen-fixing bacteria<sup>16</sup>. Also, rhizosolenid mats are capable of buoyancy regulation, allowing them to sink to withdraw nitrogen from the nutricline and rise to higher levels within the euphotic zone to photosynthesize<sup>5</sup>. A further adaptation to stratified waters in several species of large or colonial diatoms, including rhizosolenids, enables them to bloom in low-light conditions near the lowermost part of the euphotic zone<sup>17</sup>.

Given their characteristic low abundance in stratified oligotrophic waters, how then do these diatoms become concentrated to form monospecific laminae representing massive flux? The excellent preservation of the delicate rhizosolenid frustules attests to rapid deposition. We therefore require a mechanism to account

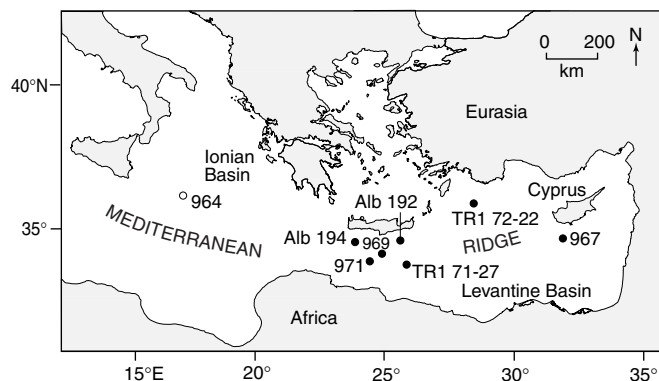


**Figure 1** Summary map of the eastern Mediterranean. The location of the relevant ODP Leg 160 sites and other cores containing diatomaceous sapropels<sup>10</sup> are indicated. Filled symbols indicate sites that contain diatomaceous sapropels, including ODP Sites 967, 969 and 971.

for both the concentration of rhizosolenids and their rapid mass-sinking. Mass concentration<sup>6</sup> and sinking<sup>18</sup> of rhizosolenid diatom mats monitored in the equatorial Pacific, and vast Neogene *Thalassiothrix* diatom mat deposits from the same region<sup>7</sup>, have been related to the action of tropical instability waves on the front between the South Equatorial Current and the North Equatorial Counter Current<sup>6</sup>. Such a model is unlikely to apply in the eastern Mediterranean as no frontal systems analogous to the equatorial Pacific operate across the area of occurrence of rhizosolenid deposits (Fig. 1).

An alternative mechanism for mass sinking within the annual cycle that does not require the action of fronts may be surmised from a recent synthesis of the timing of massive rhizosolenid diatom flux (which generally occurs in the autumn–winter<sup>19</sup>) together with recent studies of Gulf of California sediments. The seasonal flux pattern of diatomaceous laminae recorded in S5 resembles that documented by sediment-trap data<sup>20,21</sup> and BSEI analysis<sup>22</sup> of laminated Holocene sediments for the Gulf of California. There, a spring bloom is recorded by dominant flux of *Chaetoceros* spp. resting spores. During the period of summer stratification and minimal biogenic flux in the Gulf, diatom floras include both *P. calcar-avis* and *H. hauckii*<sup>21</sup> (as in the Mediterranean). Autumn/early-winter deposition, coinciding with breakdown of stratification, is represented by mat-forming diatoms including rhizosolenids, *Thalassiothrix* spp. mats as well as other colonial and large solitary diatoms documented by Goldman<sup>17</sup> as growing at depth in low-light conditions. Such diatoms, especially rhizosolenids, are very sensitive to water-column agitation<sup>23</sup>, and sediment massively when mixing breaks down summer stratification<sup>19,23</sup>. We therefore attribute the rhizosolenid/*H. hauckii* laminae occurring in S5 to an autumn/early-winter flux caused by the onset of mixing and breakdown of stratification in the Mediterranean. Thus the annual cycle of flux in the Mediterranean at the time of sapropel formation was dominated by fallout from winter–spring blooms, followed by protracted growth over the summer period of stratification which was terminated by massive sedimentation of diatoms at the onset of autumn/early-winter mixing (Fig. 3).

We now show how our reconstruction of the annual cycle of production and flux reconciles apparently divergent existing models of sapropel formation, and thus confirms earlier speculation of the role of diatoms by Sancetta<sup>24</sup>. There is general agreement that sapropel formation occurred during periods of enhanced freshwater runoff to the eastern Mediterranean. This occurred at times of precession minima through intensification of the summer monsoon resulting in increased discharge from the Nile<sup>25</sup> and probably also from increased influence of Atlantic-derived depressions causing elevated river discharge along the northern borderlands of the eastern Mediterranean<sup>1</sup>. This increased freshwater input led to enhanced stratification of surface waters. Nutrients imported through runoff to the eastern Mediterranean would rapidly have been recycled and trapped in a nutricline-associated halocline. These conditions were ideally suited to diatoms adapted to stratified conditions. There is evidence of the common existence of a deep chlorophyll maximum during periods of sapropel formation, both from the abundance of neogloboquadrinid foraminifera<sup>1</sup> and the coccolithophorid *Florisphaera profunda*<sup>2</sup>. On the basis of the evidence presented above, it is now clear that the dominant agent of production in this deep chlorophyll maximum and the food source for the neogloboquadrinids were diatoms. The relative contributions of production at depth (probably 100–130 m; refs 1, 2, 17) in this chlorophyll maximum and of production near the surface through vertical migration of rhizosolenid mats is uncertain. Winter mixing would have broken down stratification<sup>26,27</sup> and caused the mass sinking of rhizosolenid and *H. hauckii* diatoms which had been growing progressively through the summer. The mixing was sufficient to introduce adequate nutrients to the surface to generate conventional, near-surface blooms during winter–early spring recorded by the lamina of mixed diatom species.

To quantify palaeoproductivity and to assess the contribution from diatoms, we analysed organic carbon and biogenic silicon (Sibio) contents (Table 1). We combined these data with sedimentation rates based on the annual occurrence of lamina couplets (average thickness 550  $\mu\text{m yr}^{-1}$ ) and measurements of dry bulk density to produce flux data. Organic carbon and biogenic silicon

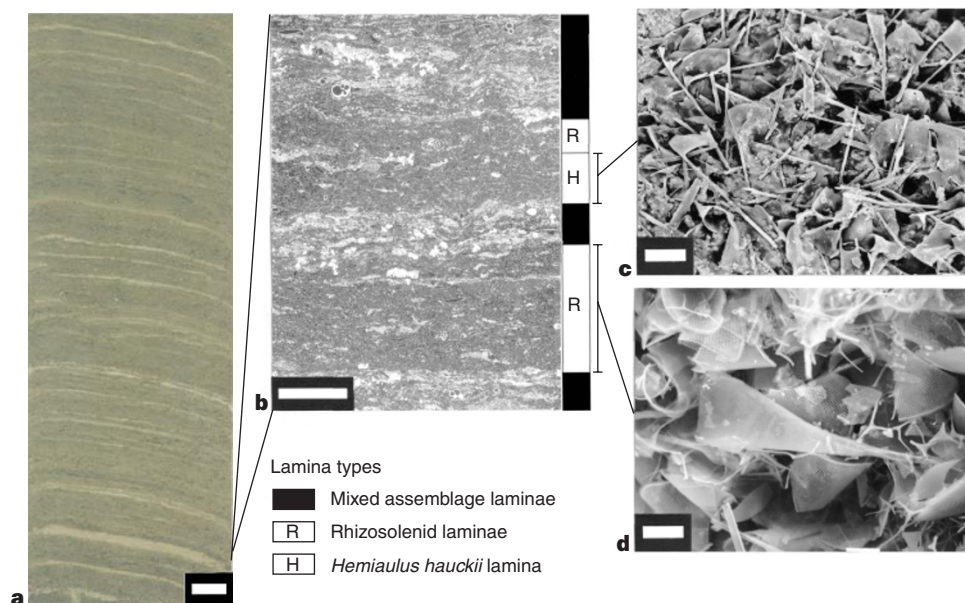


**Figure 2** Composition of the laminated sapropel. **a**, Core photograph of the laminated diatom ooze sapropel (S5), core interval 160-971C-2H-3, 81–110 cm (scale bar, 1 cm). **b**, Back-scattered electron image (BSEI) of a polished thin section of fluid-displacive resin-embedded sediment showing rhizosolenid, mixed assemblage and *H. hauckii* laminae, core interval 160-971C-2H-3, 107–110 cm. The darker-tone rhizosolenid laminae are much more porous than the

mixed-assemblage laminae as they contain a greater proportion of carbon-based resin with a low backscatter coefficient (scale bar, 1 mm). **c**, BSEI of a well preserved rhizosolenid-rich lamina (sample 160-971C-2H-3, 126–129 cm) containing *P. calcar-avis* process (centre) and girdle bands that make up the bulk of the lamina thickness (scale bar, 10  $\mu\text{m}$ ). **d**, BSEI of a *H. hauckii* sub-lamina (sample 160-971C-2H-3, 106.5–111 cm) (scale bar, 20  $\mu\text{m}$ ).



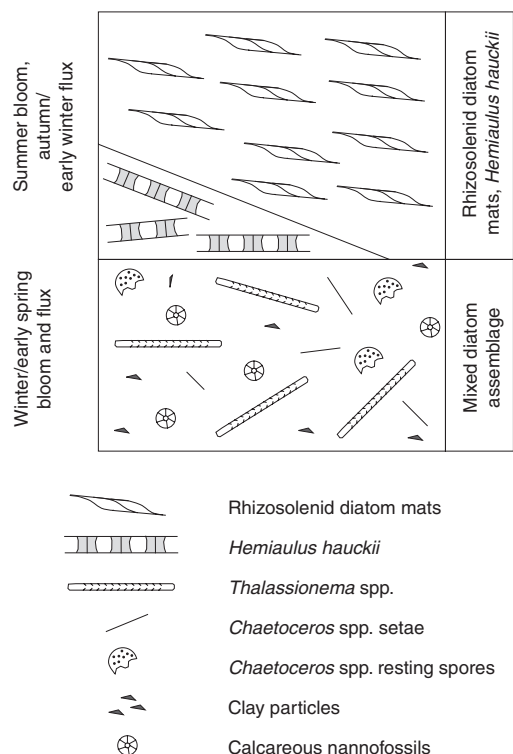


**Figure 3** Annual cycle of production and flux forming sapropel S5. Figure shows a schematic representation of the annual cycle of production and flux contained in the two-component varve common within the laminated diatom ooze of sapropel S5, Site 971, hole C. The *Thalassionema* spp. component of the mixed-assemblage laminae comprises *T. frauenfeldii* with subsidiary quantities of *T. nitzschoides*. The rhizosolenid diatom laminae are dominated by *P. calcar-avis*.

accumulation rates range from 4.6 to 9.2 g C m<sup>-2</sup> yr<sup>-1</sup> and 28 to 95 g Si<sub>bio</sub> m<sup>-2</sup> yr<sup>-1</sup> respectively, which are comparable to modern high-productivity oceanic sites. An indication of the diatom contribution to export production and the total organic carbon content may be had by comparing an original diatom Si:C ratio (as measured by Brzezinski<sup>28</sup>) of 0.14 with the present average value in S5 (from Table 1) of 2.9. This would give an export production (due to diatoms) in the range 100–200 g C m<sup>-2</sup> yr<sup>-1</sup> (we assume minimal opal dissolution as evidenced by the excellent diatom preservation). The notional 20 times decrease in organic carbon seems a sufficiently realistic degradation within an anoxic environment (compare Black Sea organic carbon preservation of 5%; ref. 29) to suggest that the diatom contribution may account for the entire organic-carbon content of the sapropel. Sapropels that lack opal and have organic-carbon contents up to 30% may be regarded as remnant deposits in which the organic carbon has been concentrated by opal dissolution.

The crucial role of diatoms in sapropel formation was inferred by van Os *et al.*<sup>26</sup>, who cite the late Pliocene, Cretan and Sicilian rhythmic diatomites, which are coeval with sapropels in the Mediterranean basin, as evidence of original diatom content. The intermittent preservation of opal in sapropels appears to be more common in the most tectonically active areas, where the periodic formation of topographic depressions may foster the development of anoxic basins (for example, the Mediterranean ridge). Our investigations of sapropels from local topographic highs such as Site 964 on the Pisano plateau (Fig. 1) show no opal preservation<sup>9</sup>.

The implications of this study apply to earlier geological times and are relevant outside the Mediterranean basin. There has been a tendency to interpret evidence of high diatom production as upwelling-related, both in earlier studies of the Mediterranean

**Table 1** Opal and carbon determinations

Dataset	Sample number	Lamina number(s) comprising each sample*	Cont.†	Si <sub>bio</sub> (%)‡	Opal (%)§	TOC (%)
1	1	79–80	P	10.31	24.74	NA
	2	72–76	P	13.83	33.18	NA
	3	67–71	P	11.55	27.72	NA
	4	62–66	P	9.90	23.77	NA
	5	62–66	P	8.15	19.57	NA
	6	58–66	P	10.82	25.96	NA
	7	50–59	P	9.43	22.64	NA
	8	42–50	P	12.43	29.84	NA
	9	38–41		16.24	38.97	NA
	10	34–36		12.67	30.40	NA
	11	31–36		15.65	37.57	NA
	12	25–31		14.87	35.68	NA
	13	22–27		24.15	57.96	NA
	14	15–21		13.13	31.50	NA
	15	9–14		13.98	33.56	NA
	16	6–10		12.90	30.97	NA
	17	1–5	P	7.23	17.35	NA
2	24	188–242		16.14	38.74	3.95
	25	172–187	P	13.07	31.37	3.83
	26	163–171		15.58	37.40	3.61
	27	156–162	D	6.48	15.55	2.75
	28	155	P	13.70	32.89	5.60
	29	127–154	P	12.50	30.01	4.73
	30	109–126	D	8.77	21.04	5.24
	31	82–108	P	13.26	31.82	5.36
	32	79–80	P	11.61	27.85	3.44
	33	28–77	P	13.12	31.49	4.95
	34	5–27		15.65	37.56	4.43

\* Lamina subdivision was on the basis of changes in diatom composition. Sample intervals were determined by the ease with which individual laminae could be identified in core section.

† Contamination: P, possible contamination by terrigenous laminae; D, definite contamination by terrigenous laminae.

‡ Biogenic silicon.

§ Opal (SiO<sub>2</sub>·0.4H<sub>2</sub>O) = 2.4 × Si<sub>bio</sub>(Si) (ref. 32).

|| Total organic carbon. The biogenic silicon determination was undertaken using a wet-alkaline extraction technique, organic carbon was measured by combustion using a Carbo Erba elemental analyser. NA, not available.

sapropels<sup>10</sup> and in the interpretation of Palaeogene and Cretaceous diatomites<sup>30</sup>, yet examination of the diatoms involved suggests an alternative explanation. In fact, both rhizosolenids and the genus *Hemiaulus* were diverse and common components of Palaeogene and Late Cretaceous diatom floras<sup>30</sup>. It follows that these diatoms grew under conditions of sustained seasonal stratification, rather than in response to upwelling. Furthermore, the sapropels resemble the rhythmic black shales of the Cretaceous, which also typically occur at frequencies associated with orbital precession or eccentricity, and which have been related to monsoonal periods of enhanced runoff carried by rivers<sup>31</sup>. Although diatoms are rarely preserved in sediments of Cretaceous age, it may be that, as with the Mediterranean sapropels, diatom production contributed to the organic-rich nature of these sediments and to the genesis of other petroleum source rocks. □

Received 17 August 1998; accepted 7 January 1999.

- Rohling, E. J. Review and new aspects concerning formation of the Mediterranean sapropels. *Mar. Geol.* **122**, 1–28 (1994).
- Castradori, D. Calcareous nannofossils and the origin of eastern Mediterranean sapropels. *Paleoceanography* **8**, 459–471 (1993).
- Calvert, S. E., Nielsen, B. & Fontugne, M. R. Evidence from nitrogen isotope ratios for enhanced productivity during formation of eastern Mediterranean sapropels. *Nature* **359**, 223–225 (1992).
- De Lange, G. J. *et al.* Composition of anoxic hypersaline brines in the Tyro and Bannock Basins, eastern Mediterranean. *Mar. Chem.* **31**, 63–88 (1990).
- Villareal, T. A., Altabet, M. A. & Culver-Rymasz, K. Nitrogen transport by vertically migrating diatom mats in the North Pacific Ocean. *Nature* **363**, 709–712 (1993).
- Yoder, J. A., Ackleson, S., Barber, R. T., Flamant, P. & Balch, W. A. A line in the Sea. *Nature* **371**, 689–692 (1994).
- Kemp, A. E. S. & Baldauf, J. G. Vast Neogene laminated diatom mat deposits from the eastern equatorial Pacific Ocean. *Nature* **362**, 141–143 (1993).
- Pearce, R. B. *et al.* A lamina-scale, SEM-based study of a diatom-ooze sapropel from the Eastern Mediterranean (ODP Leg 160). *Proc. ODP Sci. Res.* **160**, 333–348 (1998).
- Kemp, A. E. S., Pearce, R. B., Pike, J. & Marshall, J. E. A. Microfabric and microcompositional studies of Pliocene and Quaternary sapropels from the eastern Mediterranean. *Proc. ODP Sci. Res.* **160**, 349–364 (1998).

10. Schrader, H. J. & Matherne, A. Sapropel formation in the eastern Mediterranean sea: evidence from preserved opal assemblages. *Micropalaeontology* **27**, 191–203 (1981).
11. Pagou, K. & Gotsis-Skretas, O. A comparative study of phytoplankton in S. Aegean, Levantine and Ionian Seas during March–April. *Thalassographica* **13**, 13–18 (1990).
12. Ignatiades, L., Georgopoulos, D. & Karydis, M. Description of the phytoplanktonic community of the oligotrophic waters of the SE Aegean Sea (Mediterranean). *Mar. Ecol.* **16**, 13–26 (1995).
13. Alldredge, A. L. & Gotschalk, C. C. Direct observations of the mass flocculation of diatom blooms: characteristics, settling velocities and formation of diatom aggregates. *Deep-Sea Res.* **36**, 159–171 (1989).
14. Grimm, K. A., Lange, C. B. & Gill, A. S. Self-sedimentation of phytoplankton blooms in the geologic record. *Sedim. Geol.* **100**, 151–161 (1997).
15. Guillard, R. R. L. & Kilham, P. In *The Biology of Diatoms* (ed. Werner, D.) 372–469 (Botanical Monogr. 13, Univ. California Press, Berkeley, 1977).
16. Villareal, T. A. Nitrogen-fixation by the cyanobacterial symbiont of the diatom genus *Hemiaulus*. *Mar. Ecol. Prog. Ser.* **76**, 201–204 (1991).
17. Goldman, J. C. Potential role of large oceanic diatoms in new primary production. *Deep-Sea Res.* **140**, 159–168 (1993).
18. Smith, C. R. *et al.* Phytodetritus at the abyssal seafloor across 10° of latitude in the central equatorial Pacific. *Deep-Sea Res.* **43**, 1309–1338 (1996).
19. Sancetta, C., Villareal, T. & Falkowski, P. Massive fluxes of Rhizosolenid diatoms: a common occurrence? *Limnol. Oceanogr.* **36**, 1452–1457 (1991).
20. Thunell, R., Pride, C., Tappa, E. & Muller-Karger, F. Varve formation in the Gulf of California: Insights from time series sediment trap sampling and remote sensing. *Quat. Sci. Rev.* **12**, 451–464 (1993).
21. Sancetta, C. Diatoms in the Gulf of California: Seasonal flux patterns and the sediment record for the last 15,000 years. *Paleoceanography* **10**, 67–84 (1995).
22. Pike, J. & Kemp, A. E. S. Early Holocene decadal-scale ocean variability recorded in Gulf of California laminated sediments. *Paleoceanography* **12**, 227–238 (1997).
23. Richardson, T. L., Ciotti, A. M., Cullen, J. J. & Villareal, T. A. Physiological and optical properties of *Rhizosolenia formosa* (Bacillariophyceae) in the context of open-ocean vertical migration. *J. Phycol.* **32**, 741–757 (1996).
24. Sancetta, C. Mediterranean sapropels: Seasonal stratification yields high production and carbon flux. *Paleoceanography* **9**, 195–196 (1994).
25. Rossignol-Strick, M., Nesteroff, V., Olive, P. & Vergnaud-Grazzini, C. After the deluge; Mediterranean stagnation and sapropel formation. *Nature* **295**, 105–110 (1982).
26. Van Os, B. J. H., Lourens, L. J., Hilgen, F. J., De Lange, G. J. & Beaufort, L. The formation of Pliocene sapropels and carbonate cycles in the Mediterranean: diagenesis, dilution and productivity. *Paleoceanography* **9**, 601–617 (1994).
27. Tang, C. M. & Stott, L. D. Seasonal salinity changes during Mediterranean sapropel deposition 9,000 years B.P.: evidence from isotopic analyses of individual planktonic foraminifera. *Paleoceanography* **8**, 473–493 (1993).
28. Brzezinski, M. A. The Si:C:N ratio of marine diatoms: interspecific variability and the effect of some environmental variables. *J. Phycol.* **21**, 347–357 (1985).
29. Arthur, M. A. *et al.* Varve calibrated records of carbonate and organic carbon accumulation over the last 2000 years in the Black Sea. *Glob. Biogeochem. Cycles* **8**, 195–217 (1994).
30. Dell'Agnes, D. J. & Clark, D. L. Siliceous microfossils from the warm late Cretaceous and early Cenozoic Arctic Ocean. *J. Paleontol.* **68**, 31–47 (1994).
31. Jacobs, D. K. & Sahagian, D. L. In *Sequence Stratigraphy and Depositional Response to Eustatic, Tectonic and Climatic Forcing* (ed. Haq, B. U.) 329–366 (Kluwer, Dordrecht, 1995).
32. Mortlock, R. A. & Froelich, P. N. A simple method for the rapid determination of biogenic opal in marine sediments. *Deep-Sea Res.* **36**, 1415–1426 (1989).

Supplementary information is available on Nature's World-Wide Web site (<http://www.nature.com>) or as paper copy from the London editorial office of Nature.

Acknowledgements. We acknowledge funding from the NERC ODP research grant and research fellowship programme.

Correspondence and requests for materials should be addressed to A.E.S.K. (e-mail: [aesk@soc.soton.ac.uk](mailto:aesk@soc.soton.ac.uk)).

## Low-temperature thermal generation of hydrocarbon gases in shallow shales

Devon Rowe & Atis Muehlenbachs

Department of Earth and Atmospheric Sciences, University of Alberta, 1-26 ESB, Edmonton AB T6G 2E3, Canada

The thermal generation of hydrocarbon gases in sedimentary systems is generally thought to be an exclusively high-temperature process<sup>1</sup>, although previous work has indicated that significant generation may take place at burial temperatures as low as 65°C (ref. 2). Here we present the carbon-isotope signatures of gases from the Western Canadian sedimentary basin. The isotope data show that low-temperature thermal generation of non-methane hydrocarbons occurs at temperatures lower than 62°C and possibly as low as 20°C. We can distinguish between gases of shallow<sup>3,4</sup> and deep origin by using the carbon-isotope compositions of the non-methane components (ethane, propane and butane); the shallow gases have isotopic compositions consistent

with a thermal origin, whereas the deep gases—although of abiogenic origin—bear isotopic signatures that have been biologically altered. These findings have allowed the development of a successful tool for detecting the source of leaking gases around oil wells in this basin, enabling cheaper and more effective remediation.

The Upper Cretaceous Colorado Group of the Western Canadian sedimentary basin (WCSB) is a sequence of marine shales that vary in total organic content from 4 wt% to 12 wt% (ref. 5). Beneath the Colorado Group lies the Mannville Group, which consists of heavy-oil bearing sands with interbedded shales, siltstones and fine-grained sandstones. The predominant gas within these two Groups is methane (CH<sub>4</sub>), with small amounts of ethane (C<sub>2</sub>H<sub>6</sub>), propane (C<sub>3</sub>H<sub>8</sub>) and butane (C<sub>4</sub>H<sub>10</sub>) being present (Table 1). Major erosional events have removed sediments from above the Colorado and Mannville Groups since their maximum burial period; hydrocarbon generation would probably have occurred before these erosional events. Present-day conditions (depth and temperature), therefore, are not representative of the true generation conditions. Optical properties (vitrinite reflectance) of buried coal can be used to gauge the thermal maturity of the organic matter and hence to estimate maximum burial depths. Published vitrinite-reflectance values ranging from 0.3% to 0.4% indicate that the Mannville Group is thermally immature<sup>6,7</sup>. The Colorado Group does not contain coal for direct measurement of vitrinite reflectance, but an estimate can be made from established vitrinite-reflectance depth gradients in the area and from a measured value for vitrinite reflectance from within the Mannville Group (one sample from 556 m in our study area has a value for vitrinite reflectance of 0.39%). This data point, combined with the gradients published in ref. 6, results in estimates for vitrinite reflectance of 0.25–0.3% for the Colorado Group. These values reflect the combined effects of the present-day burial and the extra sediments that have been eroded.

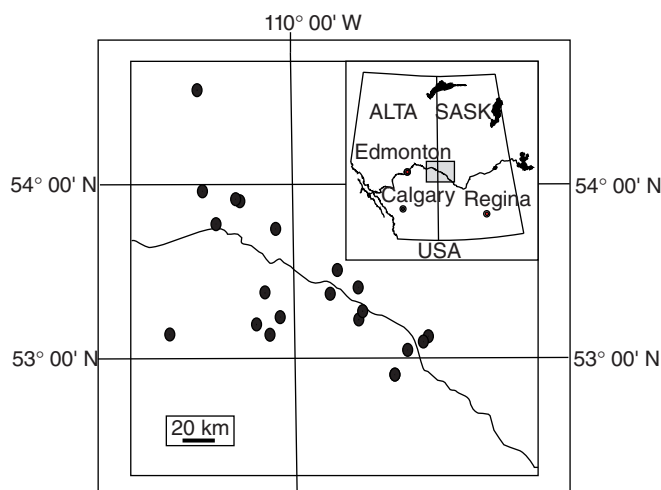


**Figure 1** Study area in the Western Canadian sedimentary basin, Canada. The location of 20 sites at which shallow natural gases were collected. At each location, drilling mud was collected as it exited the drill stem at the surface. Each well was drilled overbalanced, and sampling intervals were at roughly every 50 m. The mud (which contained fresh water and cuttings from the drill bit) was collected in 1-litre plastic containers as it exited the drill pipe (that is, at the shale shaker). A headspace was left in each container for gases held within the fluid to occupy. The 'mud gases' were heated and agitated to liberate them from solution before extracting the headspace gas for analysis of bulk gas and carbon-isotope composition (Table 1). The  $\delta^{13}\text{C}$  values (relative to Pee Dee Belemnite (PDB) standard) of the hydrocarbons were determined using a Finnigan MAT 252 (ConFlo II) continuous-flow isotope-ratio mass spectrometer, with precisions of  $\pm 0.2\%$  for methane and ethane and  $\pm 0.3\%$  for propane and butane. Data from the well indicated with an arrow are shown in Fig. 2 and Table 1.